B. Inline skating supplement

Supplementary information about the inline skating experiments and analyses are contained in the following Appendix. The material within should be read in conjunction with material from Chapter 5 of a thesis by Matthew Brodie titled: 'Development of Fusion Motion Capture for the Optimisation of Athlete Performance in Alpine Ski Racing'. References to figures and equations, where possible, refer to the originals contained in the thesis.

1.1. The Biomechanical Man - IMU to body segment mapping

Below contains an extended discussion of Section 5.1.1.1 under the same title as above.

The Biomechanical Man, a fifteen-segment body model of the athlete was constructed using the 3D anthropometric frame and the methods presented in Chapter 4. The inertial parameters of the body model were scaled from the athlete's measured characteristic limb lengths and body mass (68kg). Ten IMUs were used in the motion capture. The five body segments without IMUs were the hands, feet and head, whose movements were determined by the IMUs attached to the forearms, shanks and thorax respectively.

The IMUs were mapped to each segment using a similar process to that used for the Animating Nancy experiment in Chapter 2, but there was one difference:

- The IMU global coordinate system required a heading correction, a rotation about the global vertical or Z-axis, from magnetic north (IMU coordinate system global X-axis) to the global X-axis of the gymnasium coordinate system (long length of the course).

To make the heading correction an additional measurement was needed. The solution was to manually align the anthropometric frame axes with the axes of the gymnasium. Then the orientation of the athlete's sacrum, fixed by the anthropometric frame, together with the orientation of the IMU attached to the sacrum, to make the heading correction. Heading refers to the projection of a three-dimensional vector onto the horizontal plane.

To make the required heading correction it was assumed the negative z-axis of the sacrum IMU was coincident with the heading of the local x-axis of the sacrum body segment. The assumption was made because the sensor was attached to the sacrum between the posterior superior iliac spines. The negative z-axis of the IMU was measured in the IMU global coordinate system. The x-axis of the sacrum body segment was measured in the 3D anthropometric frame coordinate system, which was equivalent to the global gymnasium coordinate system as a result of the manual placement of the 3D anthropometric frame. Therefore, using the negative z-axis of the sacral IMU and the x-axis of the sacrum body segment the required heading correction between the IMU global coordinate system and the gymnasium global coordinate system could be calculated. The same heading correction was then applied to all the body segments. It was also assumed that the magnetic field in the 3D anthropometric frame was uniform, which seemed reasonable because the frame was made from non-magnetic material.

These heading corrections to the IMU to body segment mapping were consistent with the heading corrections applied to the FMC data during the skating trials because the fusion algorithm used the known gate locations (in the gymnasium coordinate system) and timings to automatically make the required heading correction. The inline skating fusion algorithm used a similar process for heading correction as used successfully in the wand experiment in Chapter 4. If the heading corrections had not been made to the IMU to body segment mapping, or there had been errors, then the athlete's global motion would have been inconsistent with his local motion, and in the resulting animations he might have, for example, appeared to be skating sideways instead of forwards.

1.2. Creating the data driven animations from FMC data

Below contains an extended discussion of Section 5.1.1.2 under the same title as above.

Several MATLAB algorithms were developed to visualise the FMC data in different ways. The processes were very similar to rendering the biomechanical man, already described in Chapter 4. However, this time the biomechanical man's movements were driven by real skating data. The animations produced were saved as movie files in compressed form using the Cinepak codec (Radius co). This allowed the data to be viewed in Windows Media player without any special software. However, some image quality was lost and the file sizes were increased.

The representations of the athlete's movement increased in sophistication with each experiment in MATLAB. First only the local movement was animated from a fixed view point using the **`view()`** function in MATLAB to view the motion that was displayed within a set of **`axes()`** in a **`figure()`**. MATLAB has a comprehensive help library where more details about these terms can be obtained. In this thesis when **`code characters`** are used it denotes actual variables or functions used in the MATLAB algorithms.

The next step was to define the environment, including the gymnasium floor and marker cones. In all cases the **`patch()`** function was used to draw coloured planar surfaces (called faces in MATLAB) between the known vertices of each graphical object. The gymnasium floor was flat and so was completely defined by four points defining the four gymnasium corners. The eight sided **`Local_Cone_Points`** graphic was constructed in a local reference frame. The cone vertices were defined by eight evenly spaced points around a circle of radius 0.15 metres and one central point 0.5 metres above the origin. The eight cone faces each connected two consecutive points on the circle edge and the central point. The global **`Cone_Points`** graphic was then created by moving the **`Local_Cone_Points`** into global coordinates by shifting the underlying circle origin to the measured position of each cone on the course. The visual representation of the cones can be seen in Video 1.

It was possible to display the data in a way that might be more congruent with the athlete's perception of the motion than the fixed external view point often provided by a video camera. The

virtual camera position was based on bony landmarks of the athlete's head. The camera target was the cervical joint centre. The virtual camera position was fixed 15 metres behind the athlete on a vector connecting the athlete's sellion and base of skull. The roll angle of the camera was defined by the vector connecting the athlete's vertex and cervical joint centre.

Circular shadows representing the athlete's centre of mass (CoM) and feet locations were projected on the floor, which improved the visual connection between the athlete's movements and his environment. Finally, the athlete's CoM velocity vector was used to define the camera position. These results are presented later on.

1.3. Additional results from data visualisation

An additional data visualisation shows the global motion was combined with the local motion (Video 1).

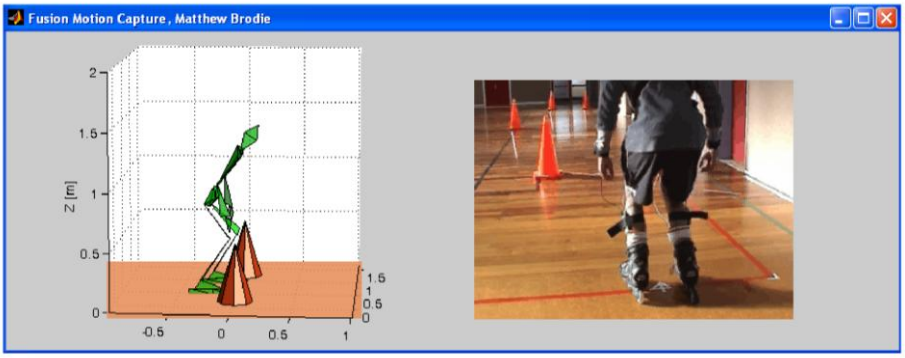

Video 1: FMC Video/Skate_Global_Video_V1.avi

1.4. Additional discussion about GRF calculations

Below contains some additional discussion about some assumptions required to calculate the ground reaction forces acting on the athlete during inline skating.

The calculation of ground reaction force magnitudes (Equations 5.8 and 5.9 of the thesis) gave unreliable results when the denominators were near zero. This happened when the skate soles were nearly normal to the CoM velocity vector. The situation only occurred when the athlete did a stationary synchronisation jump at the start and arose because the insole system could not measure the horizontal shear forces. For the purposes of obtaining a robust solution the angles between the vector perpendicular to the skate soles and the CoM velocity vector (θ_L and θ_R) were limited to less than 85º. This prevented the denominator from becoming too close to zero and the measurement noise becoming exacerbated when the athlete was airborne.

Two further assumptions were made. Firstly, the insole pressure data were assumed to give an accurate estimation of the ratio of ground reaction force magnitudes perpendicular to each skate sole. This ignored the forces transferred through the skate shank, and assumed the RS-Scan insole was capable of accurately measuring the loading ratio. Secondly, the skate orientation and hence

the ground reaction force direction vector was assumed to be accurate. The skate orientation was estimated from the IMU attached to the athlete's shank as previously discussed in the thesis. Better results might have been possible if additional IMUs had been attached directly to the skates to give orientation. Neither assumption was desirable, but both assumptions were acceptable in order to obtain results.

1.5. Dissipative force calculations: Wind drag and bearing friction

Additional information for this section is provided below.

Selection of model coefficients

To reduce the ratio of measurement noise relative to the athlete's motion, and reduce the effects of statistical outliers, only data from periods when the athlete was travelling faster than $1.8ms^{-1}$ were used to calculate the coefficients of wind drag and bearing friction. This removed from the analysis the noisy data from the synchronisation jump and end braking periods, but included nearly all the skating data.

Residual force calculations and ground reaction forces

After the dissipative forces had been modelled, there were still small residual forces that were assumed to be a result of non-linear bearing friction, changes in the athlete's frontal area, or errors in the measurement of skate orientation. The residual forces were treated in two ways depending on if the athlete was stationary or not.

During stationary periods, which were defined as a velocity of less than 0.2m/s, a static friction model was invoked. For static friction calculations the friction coefficient was defined as equal to, or as less than the dynamic friction co-efficient in order to reduce any residual forces. This prevented the static friction being greater than the applied force when the foot was stationary.

The remaining residual forces were then added to the calculated ground reaction forces divided between the two feet according the ratio as measured by insole system. This approach meant that the new ground reaction forces contained most of the information that separated the technique of one run from another. It also meant that the sum of the external forces matched the resultant force calculated from the athlete's CoM acceleration. A disadvantage of this approach was that reduced wind drag from reduced frontal area could have been misinterpreted as increased ground reaction forces accelerating the athlete.

Component energy calculations

While the power developed by each external force shows the instantaneous effect on the resultant CoM motion an energy analysis shows the net contribution of a particular force over entire courses, or sections of the courses.

Energy changes or work done by the external forces are calculated by the integral of the power. In this way different external forces that change over the course can be given a scalar value describing the energy contribution to the motion in Joules. A positive energy means that the force has done work that has acted to increase the athlete's kinetic energy, and therefore the athlete's velocity over the course. When integrating the power to obtain energy, the reverse of the numerical differentiation process used to compute velocity from CoM position should be used to prevent numerical artefacts.

Two checks were carried out on the component energy calculations. Firstly, the gravitational energy, as calculated by integration of the gravitational power, was checked for consistency against the gravitational potential energy calculated by the athlete's mass and change in height (mass*gravity*Δheight). Secondly the kinetic energy calculated by summation of the work done by each external force was checked for consistency against the total kinetic energy calculated from the athlete's mass and velocity (1/2 *mass*velocity^2).

Visualisation of external forces and athlete speed

The visualisations presented build on those from the previous section, both the external forces and the athlete's speed were visualised. Each graphical element was drawn using the `line()` function in MATLAB, both colour coded and scaled to the underlying data. Green lines were used for forces with a positive power or accelerating forces, and red lines were used for forces with a negative power or breaking forces.

1.5.1. Results and discussions

Validation of the wind drag and bearing friction coefficients

This is an extended discussion of that provided in the thesis.

The wind drag and bearing friction were modelled by two equations requiring two coefficients of friction (K_{Drag} = 0.58Ns^{2}m^{-2} and $K_{Friction}$ = 0.016, Equations 5.10 and 5.11 of the thesis). The coefficients were chosen to minimise the residual force balance (Equation 5.1 of the thesis). But how close was this estimation to the true bearing friction and wind drag forces? The approach taken suffered from several problems.

Firstly, there were problems with the FMC system. Foot orientation was estimated from the shank IMUs, the RS-Scan insole system suffered from hysteresis (Figure 5.11 of the thesis) and the CoM trajectory from which the resultant external force was derived, may also have contained small amounts of measurement error.

Secondly, over the course it was unlikely that constant lumped coefficients (K_{Drag} and $K_{Friction}$) accurately modelled the true forces. The bearing friction did not include any non-linear bearing friction arising from torsion applied to the bearing during a skating stroke. We were also unsure if the Coulomb friction model was suitable; maybe a viscous friction model (taking account of the compression of the soft plastic wheels and incorporating velocity dependency) should have been

used as well. In any case the bearing friction coefficient used ($K_{Friction}$ = 0.016) was greater than that of ice skating (0.003-0.007, (van Ingen Schenau, 1982) but less than that of skiing on both hard and soft snow (0.04-0.2, (Shimbo, 1971) and close to the value used for roller skis on asphalt (0.021, (Spring, Savolainen, Erkkila, Hamalainen, & Pihkala, 1988).

Thirdly, the wind drag coefficient was dependant on both the cross sectional area of the athlete, which was not constant over the course, and Reynolds number. Reynolds number depends on effective wind speed. According to measurements made in a wind tunnel of speed skaters below 19ms^{-1}, the wind drag coefficient is not constant, but as wind speed increases, the wind drag coefficient decreases (van Ingen Schenau, 1982). This was attributed to the boundary air layer separating from the athlete closer to the front of the athlete at lower speeds and producing a larger wake. Schenau reported lumped wind drag coefficients of around 0.15Ns^{2}m^{-2} for speed of 12ms^{-1}, but also reported that at 5ms^{-1} (close to the maximum speed of our athlete at 4.5ms^{-1}) the lumped wind drag coefficient increased by around 2.5 times to approximately 0.40Ns^{2}m^{-2}. Our athlete also used an upright stance which was reported to further increase the wind drag coefficient by a factor of 1.2-1.5. To complicate matters further, Schenau also tested speed skaters in woollen suits at slower speeds (similar to the speeds and dress of our athlete) as well as lycra speed suits. At slow speeds (<6ms^{-1}) the woollen suits produced less drag than the lycra suits, apparently because the woollen material allowed the turbulent air flow to develop earlier in the boundary layer. Considering all these factors, the value for the average wind drag coefficient calculated in MATLAB (K_{Drag} = 0.58Ns^{2}m^{-2}) seemed well within reason.

For comparison it was also useful to convert the calculated lumped wind drag coefficient (K_{Drag} = 0.58Ns^{2}m^{-2}) into wind drag area (C_dA = 0.96m^2) and wind drag coefficient (C_d = 1.6). To make the conversion an estimate of air density (1.205kg.m^{-3}) was required along with an estimate of the athlete's cross sectional area while skating (0.6m^2) and multiplication by a factor of two. The estimates of wind drag area and wind drag coefficient were again higher than those reported in literature, but this was probably a result of the much slower speeds the subject used. A summary of previous wind drag literature is also reported in a paper by Kaps (Kaps, Nachbauer, & Mossner, 1996).

Finally, the calculated optimal solution for wind drag coefficient was negatively correlated to the bearing friction coefficient. To demonstrate the negative correlation the coefficients over several different windows of data were calculated (Figure 1). Only data corresponding to speeds above different cut offs were used to reduce the signal to measurement noise ratio, especially from motion during the start synchronisation jump. The bearing friction coefficient was multiplied by ten so both coefficients could be viewed on the same scale.

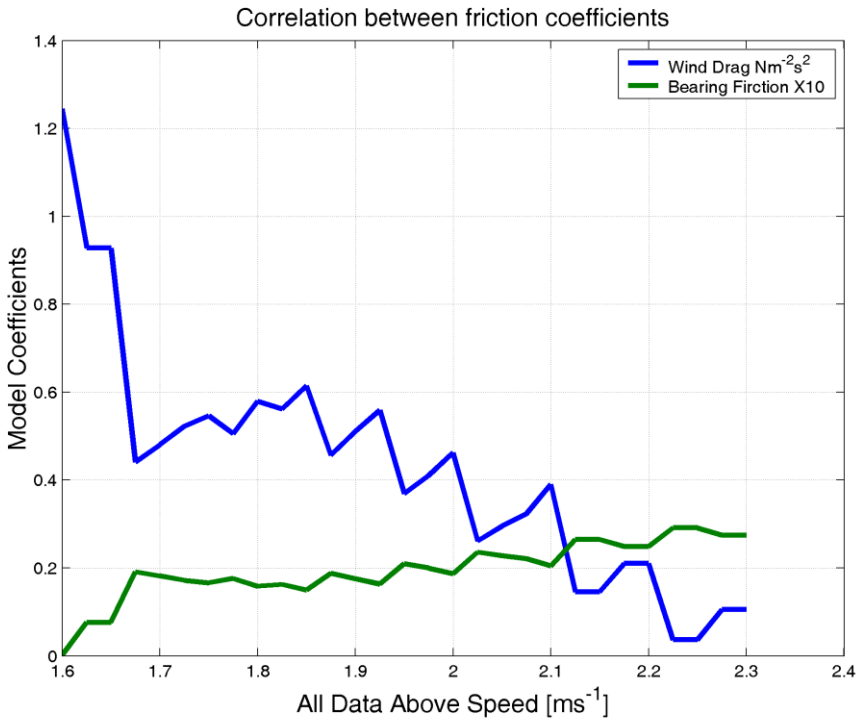

Figure 1: Range of feasible model coefficients for wind drag and bearing friction

In Figure 1 only the ranges of feasible values are graphed between cut-off speeds of 1.6-2.3ms^{-1} where both coefficients are positive. The negative correlation shows that when finding the optimal solution a smaller wind drag co-efficient can be compensated for by a larger bearing friction coefficient. If a larger range of athlete speeds had been used, more robust results might have been possible. The decrease in wind drag coefficient with increased cut-off speed might have been a result of the actual wind drag co-efficient decreasing with increasing velocity. If a better model for the wind drag coefficient had been used, more robust results might have been possible. 1.8 m/s was used as the cut off speed because it was in the middle of a relatively constant part of the graph. The optimised model coefficients used were K_{Drag} = 0.58Ns^{2}m^{-2} and $K_{Friction}$ = 0.016, but it was possible, considering the graph (Figure 1) and values reported in literature that the true mean values could have been anywhere between 0.24-0.95Ns^{2}m^{-2} for K_{Drag} and 0.007-0.022 for $K_{Friction}$. In any case the combined effect of modelled wind drag and bearing friction on the athlete's centre–of-mass trajectory remained relatively unchanged regardless of the chosen cut-off speed in the analysis because of the high negative correlation between the two coefficients.

Forces and trajectory and skating strokes

This section contains mostly new material analysing the skating strokes from the global and local perspectives.

Figure 2 shows the foot strokes from an external view point, but is this how the movements are perceived by the athlete? Probably not, so it may also be useful to analyse skate motion relative to the athlete's CoM motion (Figure 3). Figure 3 shows the left foot strokes of the athlete (thick blue line) relative to the athlete's CoM trajectory (the origin) and direction of travel (positive X-axis). In Figure 3 ground reaction forces are also visualised and colour coded. The skate strokes

generally started 0-20cm in front of the athlete and finished 20-40cm behind the athlete. Skate strokes generally started with a braking period (dark red lines) where the skate moved towards the CoM and finished with an accelerating period where the skate moved away from the CoM. Increases in speed only occurred during diverging CoM and skate trajectories. Both the inside and outside edges of the left skate were used to propel the athlete.

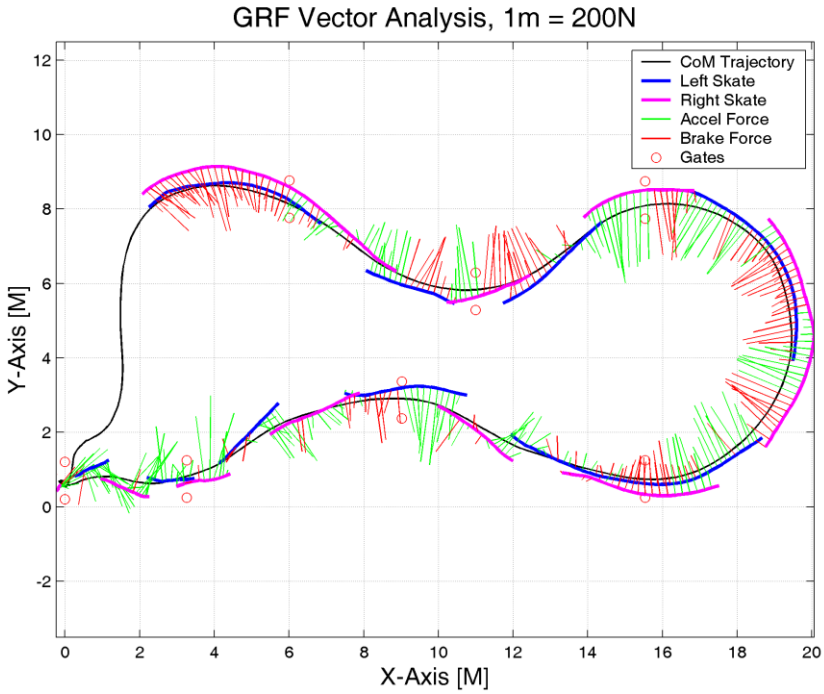

Figure 2: Ground Reaction Force vector diagram shows skate strokes

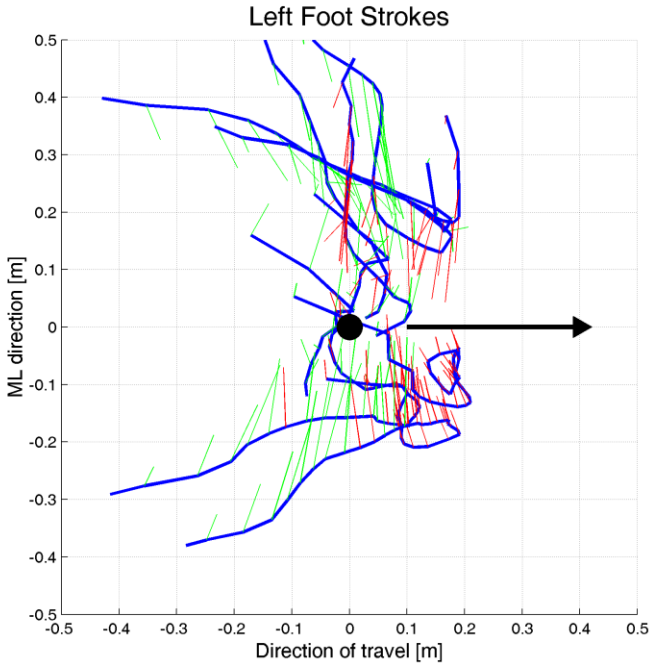

Figure 3: Left skate strokes in the athlete centred coordinate system

Figure 3 and Figure 2 show a large variety of strokes were used through the course, which may demonstrate either the athlete's versatility and/or the fact he was still experimenting to find the best skating strategy. The more parallel the skating strokes were to the direction of travel (horizontal axis, Figure 3) the more they increased the athlete's velocity. The more mediolateral the skating strokes were, the more useful they were for cornering and braking. The faster the athlete moved his skate (or end effector) relative to his CoM, the more parallel to the direction of travel the skate could move and therefore more power could be produced. Except, the force-velocity relationship of muscle meant that the faster the skate was moved, the less force could be produced and therefore less power could be produced. This meant the maximum skating power was a trade off between the force applied to the skate and the relative velocity of the skate. The optimum relative skate trajectory depended on this trade off, the CoM speed and the required task; accelerating, turning, or braking. This force velocity trade off could account for the large variety of skate strokes observed.

Validation of the power, work and kinetic energy

Below is an energy balance that closes the loop and proves the calculations were consistent with the athlete's measured motion.

All the information required to carry out an energy balance on the athlete is now available. The work done by the external forces (ground reaction, bearing friction, and wind drag) should be equal to the sum of the change in kinetic (ΔE_K) and potential energy (ΔE_P) of the athlete (Figure 4: Energy balance, skating one lap).

Equation 1 $$Work\_Done = \Delta E_K + \Delta E_P$$

Equation 2 $$\Delta E_K = \frac{m\left|\mathbf{V}_{\mathbf{CoM}}\right|^2}{2}$$

Equation 3 $$\Delta E_P = mg\Delta h$$

The energy balance (Figure 4) validates the calculation process used in the previous analyses. If there were errors in any of the previous calculation steps then these components would not balance. Energy balances may also be very useful in skiing because the loss in potential energy as the athlete travels down the mountain (ΔE_P, Equation 3) should be related to his gain in kinetic energy and velocity (ΔE_K, Equation 2).

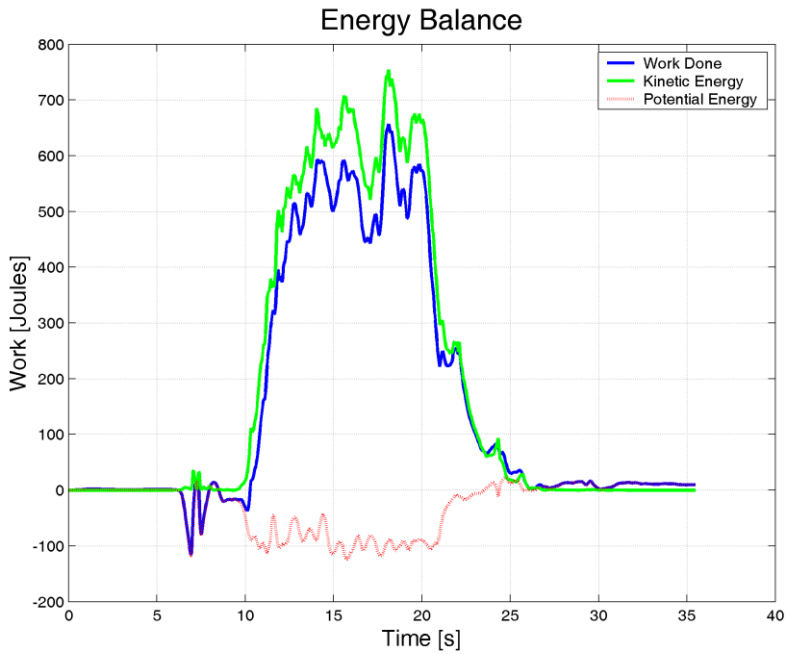

Figure 4: Energy balance, skating one lap

The promising results show that with FMC data, it is possible to calculate the effect of different external forces, wind drag, ground reaction force, bearing friction and gravity on athlete performance. Although the results contained a small amount of measurement noise, the calculations were proven to be both robust and consistent by force and energy balances. Accuracy could be improved further if IMUs were attached to the skates and if the RS-scan insoles did not suffer from hysteresis. The results are promising and the calculations were designed so they could be directly applied to skiing data in the future.

1.6. Net joint torques, inertia and whole body rotations

This section was omitted from the main body of the thesis. The calculations however, are the same as those used in the thesis to analyse skiing. Some of the results may provide an interesting comparison to the results later obtained for alpine skiing.

Is it now possible to calculate the net joint torques and powers? The net joint torques about the knee joint could provide useful information for reducing ski injuries with future data. Now the calculation procedure are investigated along with the assumptions required and the accuracy of net joint torques based on the inline skating data.

Analysing net joint torques brings the analysis one step closer to understanding which muscle groups are responsible for the athlete's local limb and global movement. Net joint powers shed light on whether the muscle groups are working eccentrically (negative power) or concentrically (positive power). Such information together with joint velocity and joint range of movement measurements may be useful to physical trainers when developing sport specific training programs, and in injury prevention.

1.6.1. Methods

Calculation of ground reaction torques

Before calculating the net joint torques at the ankle, knee and hip joints, the ground reaction torques was required (the rotating force applied to the skate by its interaction with the rolling surface). Because the ground reaction torques could not be measured by the RS-scan insole system, it was first necessary to estimate the ground reaction torques from the FMC data. Most commonly the torque was developed when the ground reaction force vector did not act directly through the ankle joint centre. Because of the skate design, the torque could also pass directly from the skate to the shank through the stiff boot upper.

It was assumed the ground reaction torques were the residual between the external torques (a consequence of the external forces not acting through the CoM) and the athlete's rate of change of angular momentum (measured from the acceleration and rotation of the local body segments about the athlete's CoM). The residual ground reaction torques were then divided between the athlete's skates according the RS-Scan measured foot loading ratio.

The calculations were done in an athlete centred coordinate system meaning all torques were calculated relative to the CoM.

Calculation of external torques

To simplify the calculations it was assumed that wind drag acted though the athlete's CoM (**CoM**) and so both wind drag and gravity produced no external torque. The external torque measured in the global coordinate frame was then calculated ($\mathbf{T_{External}}$, Equation 4) by the cross products (×) between the external forces ($\mathbf{F_{Right}}$ and $\mathbf{F_{Left}}$) and the relative displacement from the CoM of the point of force application (**CoP** – **CoM**). Both the ground reaction forces and bearing friction forces were combined and assumed to act through the CoP (**CoP**) as measured by the RS-Scan insole system but displaced 10cm along the local y-axis of the skate to account for the height of the skate wheels.

Equation 4
$$\mathbf{T_{External}} = \left(\mathbf{CoP_{Right}} - \mathbf{CoM}\right) \times \mathbf{F_{Right}} + \left(\mathbf{CoP_{Left}} - \mathbf{CoM}\right) \times \mathbf{F_{Left}}$$

Calculation of change in angular momentum ($\mathbf{T_{Internal}}$)

The rate of change in angular momentum of each limb segment was calculated and summed to get the total rate of change in angular momentum ($\mathbf{T_{Internal}}$). For each limb segment the rate of change in angular momentum was composed of a remote ($\mathbf{T_{Remote}}$) and local term ($\mathbf{T_{Local}}$). The remote term in global coordinates was calculated by the cross product between the relative distance ($\mathbf{CoM_{Limb}} - \mathbf{CoM}$) and net forces accelerating the limb's CoM ($\mathbf{A_{Limb}} * m_{Limb}$). The limb CoM ($\mathbf{CoM_{Limb}}$) acceleration ($\mathbf{A_{Limb}}$) and the athletes CoM (**CoM**) were extracted from the FMC data and the calculations were completed using a MATLAB algorithm written by the author.

Equation 5 $$\mathbf{T}_{\mathbf{Remote}} = \left(\mathbf{CoM}_{\mathbf{Limb}} - \mathbf{CoM}\right) \times \left(\mathbf{A}_{\mathbf{Limb}} * m_{Limb}\right)$$

Calculation of the local term ($\mathbf{T}_{\mathbf{Local}}$) in global coordinates was slightly more complicated. At each time step the angular momentum of the limb segments were calculated by rotating the inertia tensor ($\mathbf{I}_{\mathbf{Local}}$) and measured angular velocity ($\boldsymbol{\omega}_{\mathbf{Local}}$) of the limbs into global coordinates using the orientation matrix ($\mathbf{R}_{\mathbf{LG}}$) and then multiplying them together. The angular momentum was differentiated to get the local torque term. The rate of change in angular momentum was finally calculated from the sum of the remote and local terms for all limbs.

Equation 6 $$\mathbf{T}_{\mathbf{Local}} = \frac{d\left(\left(\mathbf{R}_{\mathbf{LG}} * \mathbf{I}_{\mathbf{Local}}\right) * \left(\mathbf{R}_{\mathbf{LG}} * \boldsymbol{\omega}_{\mathbf{Local}}\right)\right)}{dt}$$

Both the calculated torques, internal and external, for a single lap, are shown in Figure 5. The observable difference between the internal and external torque may be a result of several factors:

1. Noise and errors in the FMC system.
2. Ground reaction force torques transferred through the shell of the inline skate and bypassing the RS-Scan insole system.
3. Errors in the RS-Scan insole measurement of foot loading ratio and centre of pressure (CoP).
4. Wind drag does not act exactly through the athlete's CoM.

In Figure 5 the large step change in Y-axis external torque approximately four seconds into panel two appeared because the RS-Scan CoP measurements started after the IMU measurements. A change in CoP location of 10cm produces a change in external torque of around 70 Nm. The residual torque was assumed to be a result of torques transferred through the skate shells. The residual torque was calculated and then added to each skate. The total residual torque was divided between the skates according to the measured foot loading ratio.

Calculation of foot loading ratio by a torque balance

Could one solve for the true foot loading ratio by minimising the residual torques? (Figure 6) MATLAB's constrained nonlinear minimisation tool was used to find the foot loading ratio that minimised the residual torques. The results suggest it may be possible to accurately solve for the foot loading ratio from inverse dynamics. Figure 6 suggests the assumption that the athlete's weight was distributed evenly between the feet at the start may be slightly wrong, as the torque balance suggests he favoured his left foot. The foot loading ratio derived from the torque balance appears noisier than the RS-Scan insole measurement. There may be many reasons for this including:

1. The RS-Scan insole system filters the high frequency components.
2. The derived loading ratio is inherently noisy and needs filtering.
3. The CoP measurements used where not accurate

4. The ground reaction forces contained error because the foot orientations were estimated by IMUs attached to the athlete's shanks.
5. The body segment inertial parameters used contained error.

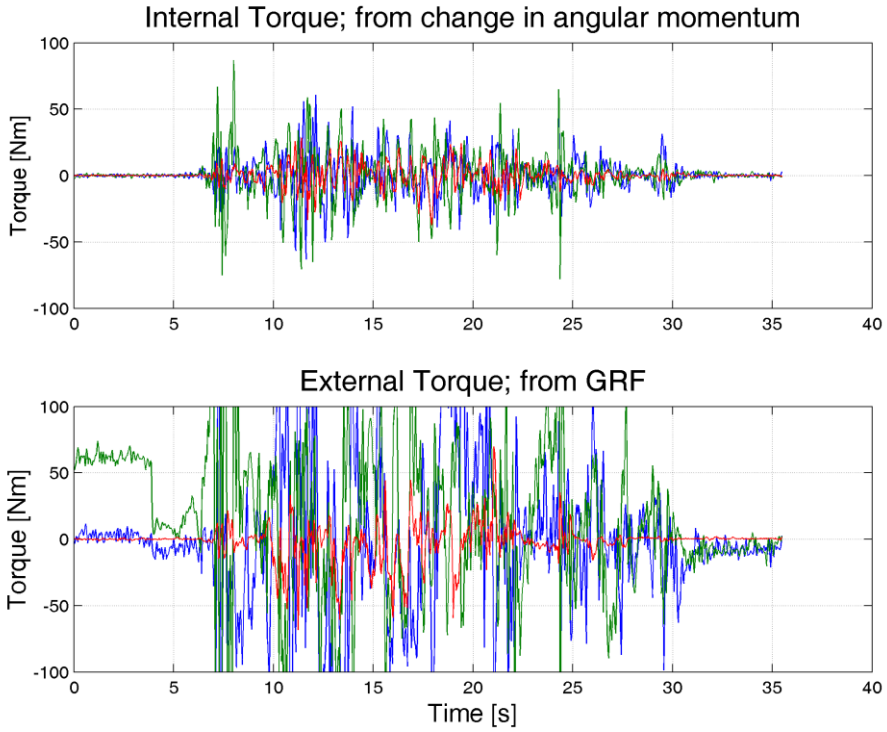

Figure 5: Torque balance in skating

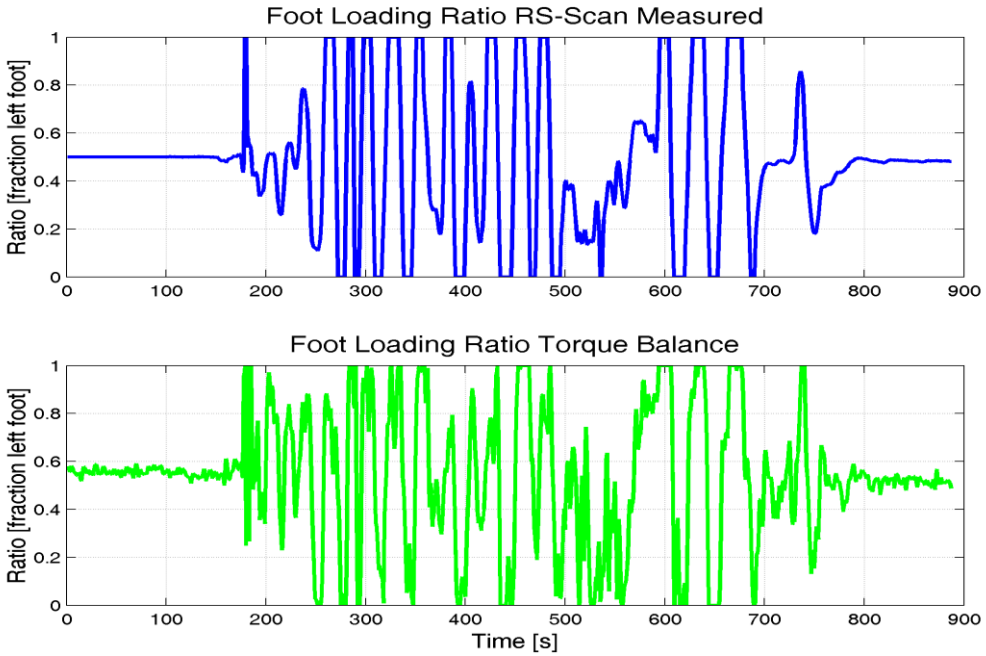

Figure 6: Comparison of foot loading ratio, measured and calculated

Calculation of net joint torques

The net joint torques were calculated in sequence from distal to proximal segments, working from the head, hands and feet inwards. The most proximal body segment was defined as the sacrum and the torques were then defined according to the right-hand rule, with the torques acting from the proximal segment on the distal segment. When the right thumb is aligned with and pointing in the same direction as the torque (little finger next to the origin at the proximal joint centre) then the curled fingers indicate the direction of action of the torque on the distal body segment. By this protocol a positive torque about the hip joints that points right along the medial lateral axis acts to rotate the thigh forwards towards the sacrum and may be defined as hip flexion in the anatomical position. But the same torque at the knee acts to rotate the shank forward and is defined as knee extension.

The first step was to calculate the net joint forces sequentially from distal to proximal body segments. In the example (Figure 7 and Equation 7) the force acting from the elbow joint centre on the forearm ($\mathbf{F}_{\mathbf{Elbow}}$) was calculated by assuming the sum of forces acting on the segment was equal to the acceleration ($\mathbf{A}_{\mathbf{Arm}}$) of the segment multiplied by the mass of the arm. It was also assumed the drag force acted through the segment CoM and it was scaled from the total drag force by the mass fraction of the forearm segment. The acceleration of the forearm was calculated by twice differentiating the measured trajectory of the forearm CoM. On the right side of Equation 7 the force acting on the hand from the wrist joint ($\mathbf{F}_{\mathbf{Wrist}}$) was added because it was equal and opposite to the force acting on the forearm from the wrist joint ($-\mathbf{F}_{\mathbf{Wrist}}$).

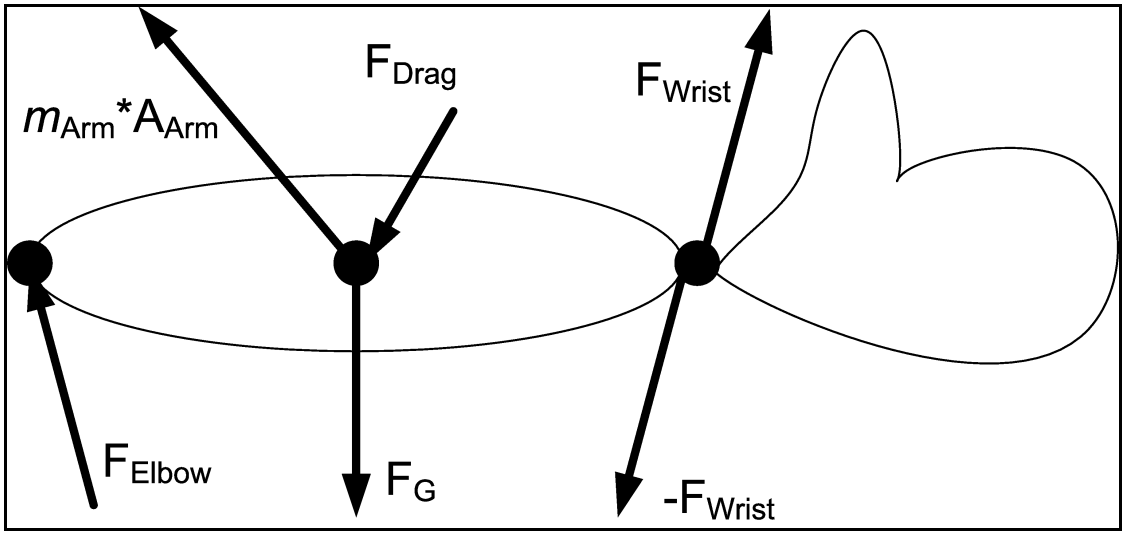

Figure 7: Force balance on the forearm

Equation 7 $$\mathbf{F}_{\mathbf{Elbow}} = m_{\mathbf{Arm}}\mathbf{A}_{\mathbf{Arm}} + \mathbf{F}_{\mathbf{Wrist}} - \mathbf{F}_{\mathbf{Drag}} - \mathbf{F}_{\mathbf{Gravity}}$$

Next the net joint torques were calculated. The net joint torques were calculated about the CoM of each body segment; the sum of torques was assumed to equal the calculated change in segment angular momentum ($\mathbf{T}_{\mathbf{Local}}$, Equation 6). In the example (Figure 8 and Equation 8) the net joint torque acting on the forearm ($\mathbf{T}_{\mathbf{Elbow}}$) from the elbow joint centre was calculated. By taking the

torques about the segment CoM, the calculation was simplified because the torques as a result of gravity and wind drag were zero. This did not affect the calculated values because the net joint torque should be the same regardless of the reference point used to calculate it.

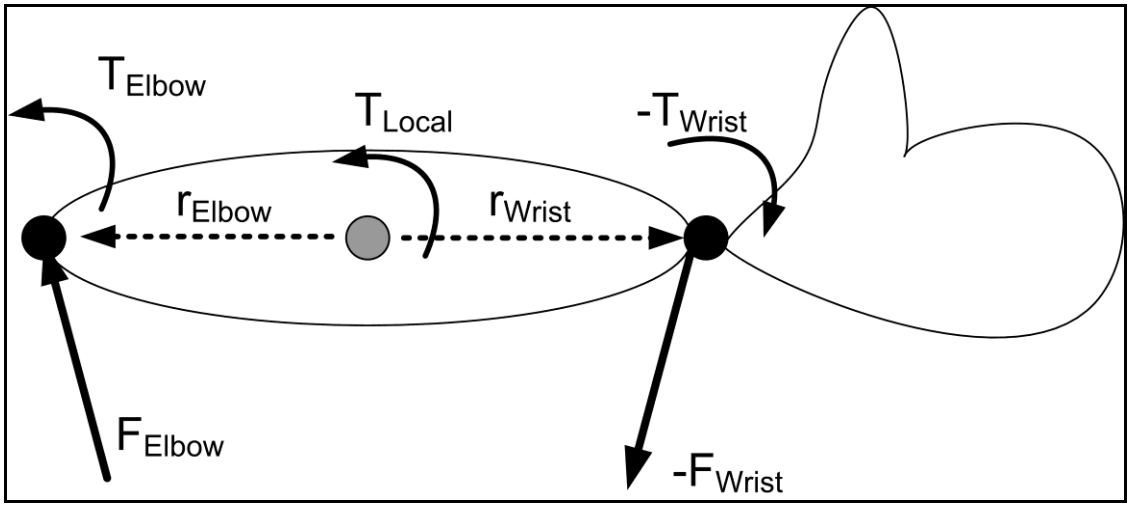

Figure 8: Torque balance on the forearm

Equation 8 $$\mathbf{T}_{\mathbf{Elbow}} = \mathbf{T}_{\mathbf{Local}} + \mathbf{T}_{\mathbf{Wrist}} + \left(\mathbf{r}_{\mathbf{Wrist}} \times \mathbf{F}_{\mathbf{Wrist}}\right) - \left(\mathbf{r}_{\mathbf{Elbow}} \times \mathbf{F}_{\mathbf{Elbow}}\right)$$

Calculation of net joint powers

Net joint powers are used to define the net mode of action of the activating muscle groups. A positive power means the muscle action is concentric; a negative power means the muscle action is eccentric.

Net joint powers were calculated from the dot product of the relative joint angular velocity and the net joint torques. The relative joint velocity was calculated by subtracting the proximal body segment angular velocity from the distal segment angular velocity; this gave the movement of the distal segment relative to the proximal segment. All calculations were performed in the global coordinate system so the results could be overlaid on the data driven animation of the athlete.

1.6.2. Results and discussion

Displaying and understanding net joint torques

The net joint torques during standing, an eccentric phase of the skate stroke, and a concentric phase of the skate stoke are shown (Figure 9 to Figure 11). All net joint torques were defined according to the right-hand rule, and animated from the proximal joint centres of the distal limbs. By this convention the ankle joint torques defined the torques acting from the shanks on the feet segments. The torques were colour coded according to the calculated net joint powers; light blue for eccentric action and dark blue for concentric action.

The first figure (Figure 9) is included to show the relative magnitude of the torques when the athlete is stationary and in a slightly crouched pose. Although both concentric and eccentric torques are shown, the mode of action is basically isometric because the relative joint motion is very small. The analysis did not include a colour code for isometric action, but in future improvements a cut-off joint velocity could be used to colour code near isometric action. The largest torque acts about the lumbar joint centre, it represents a torque acting on the thorax body segment from the sacrum. This torque is acting to extend the trunk and is counteracting the gravity force acting on the upper body to flex the trunk. The net result is very little movement of the trunk.

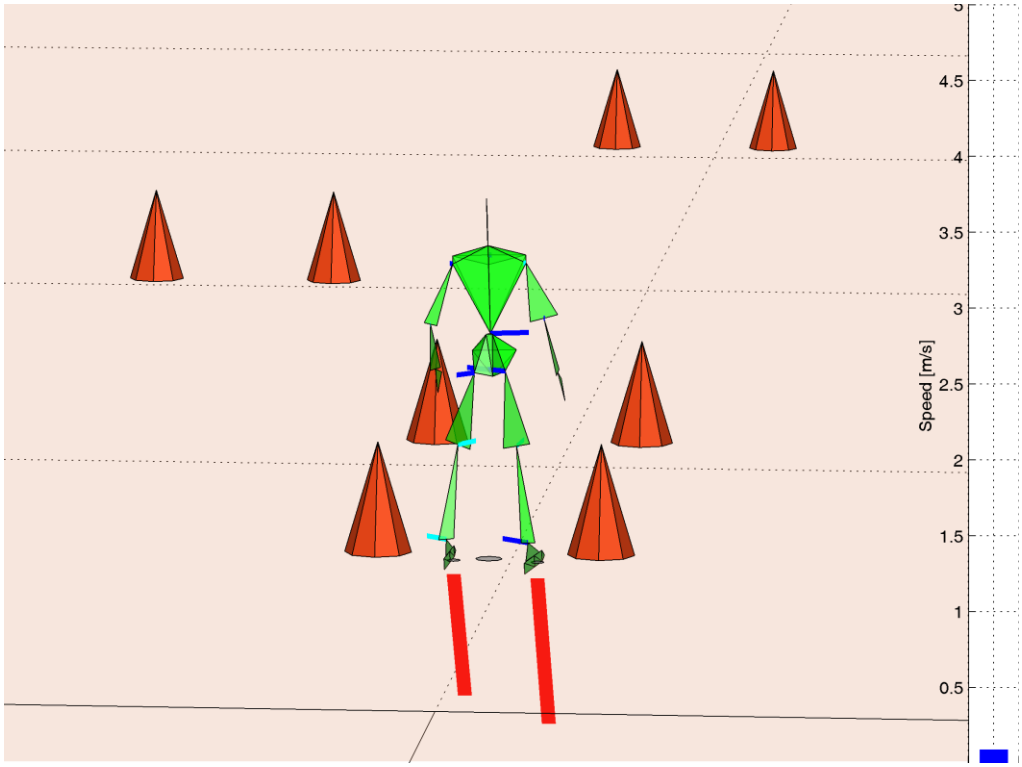

Figure 9: Isometric net joint torques while standing

The next figure (Figure 10) shows the first phase of a skating stroke, loading of the left leg. Generally there is eccentric loading (light blue torque vectors) as the muscles strongly resist the motion of the CoM as it moves left. Notice how the torques of the hip, knee and ankle act in opposite directions, but are acting to extend the leg as a result of the 'Z' configuration of the leg joints. However, the leg is not yet extending because of the momentum of the athlete's CoM is moving left and downwards. Compared to the standing pose, the torques of the loaded leg are much higher. There are only small torques acting at the upper body joint centres, but there are significant concentric torques (dark blue torque vectors) at both the right hip and knee acting to bring unloaded leg forward.

Several frames later in the middle of the concentric phase of the skating stroke (Figure 11), the loaded left leg begins to extend and propel the athlete forward and to the right. There are large concentric net joint torques acting at hip, knee and ankle (dark blue vectors).

Video 2 shows the calculated net joint torques overlaid on the data driven animation of the athlete doing a single lap through the course. Repeat viewings of the animation at a slow speed are recommended, as there is a lot of information to process. The analysis successfully calculated a plausible set of net joint torques.

Video 2: FMC Video\Skate_Rear_Torque.avi

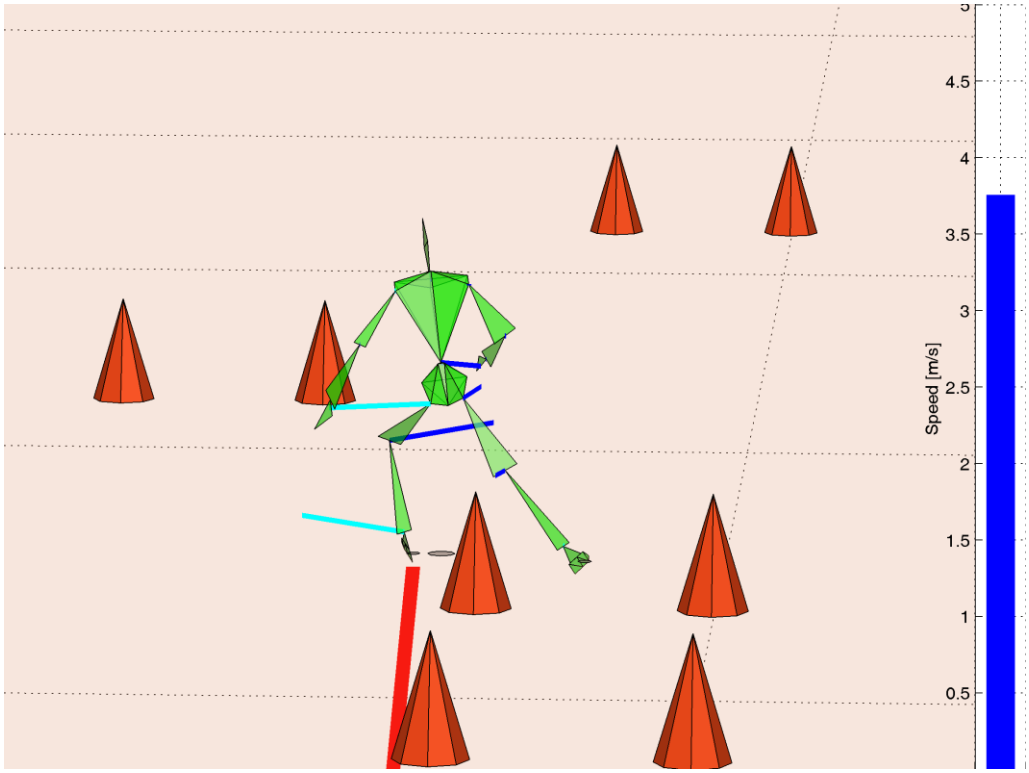

Figure 10: Eccentric loading of the left leg as the CoM moves left

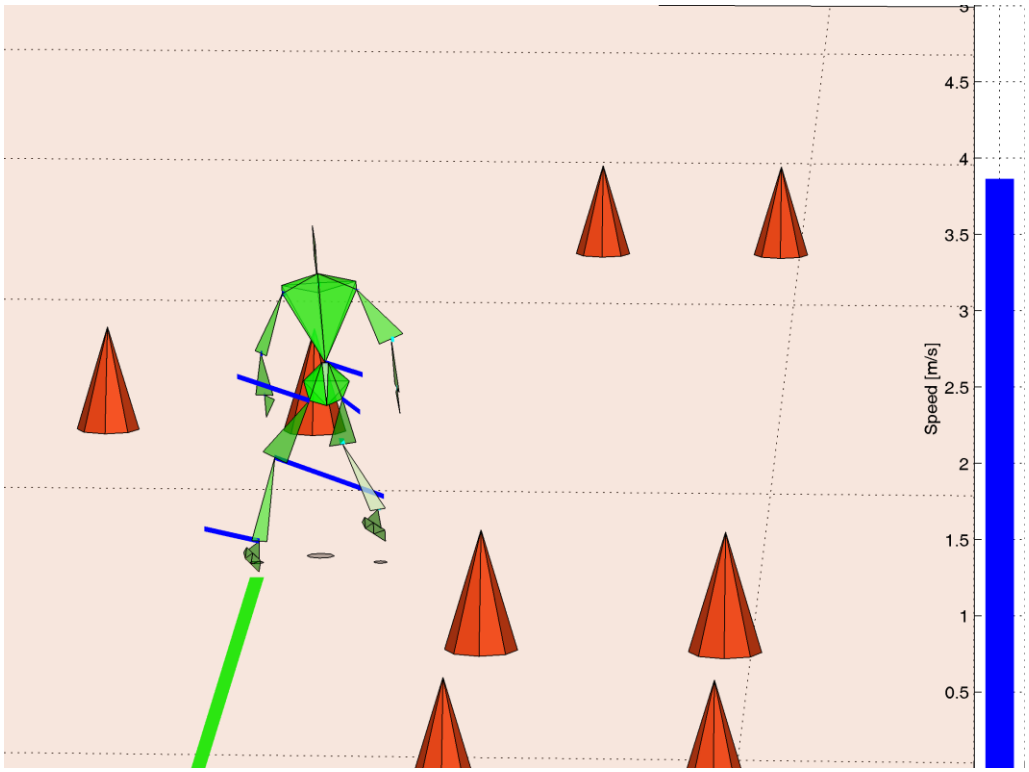

Figure 11: Concentric loading of the left leg drives the CoM right

Local dynamics of the left leg

The local dynamics of the left leg are visualised in Figure 12 and Figure 13.

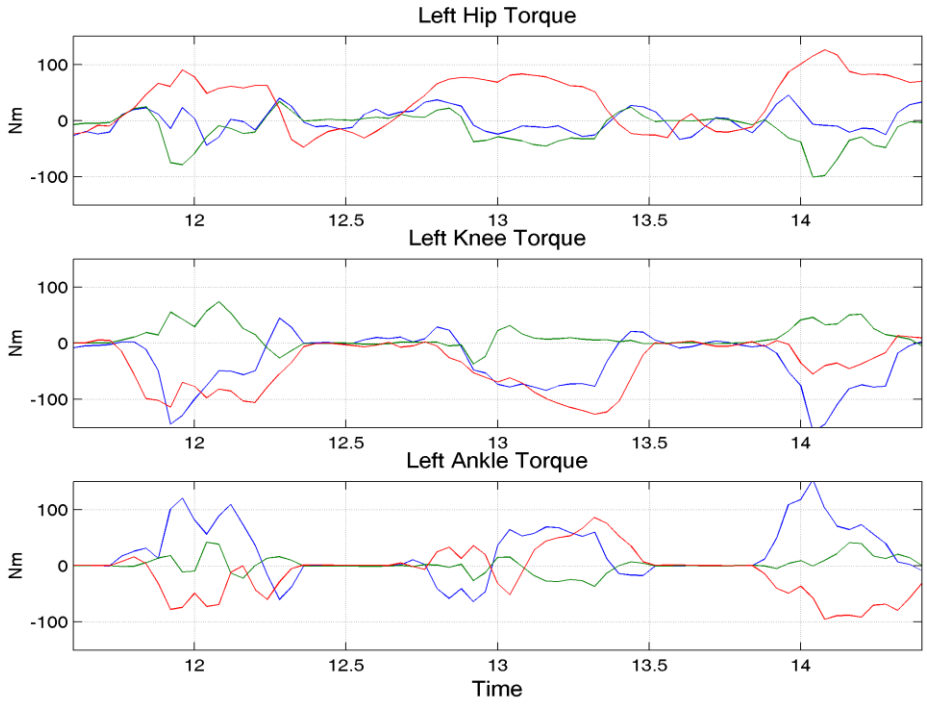

Figure 12: Left leg torques for three skating strokes

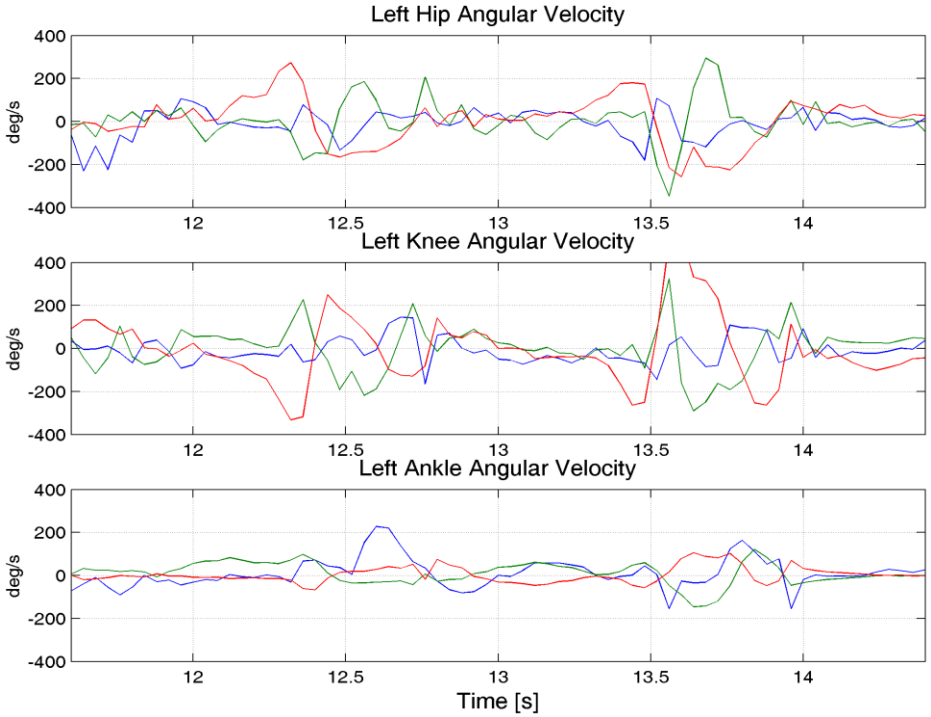

Figure 13: Left leg relative joint velocities

The net joint torques of the left leg were rotated back into the local coordinate system of the proximal body segment and graphed (Figure 12). The local limb coordinate systems were defined by our body model in Chapter 4. Generally in these coordinate systems flexion/extension takes place about the local z-axis (red line), abduction/adduction about the local x-axis (blue line) and internal/external rotation about the local y-axis (green line). The joint angular velocities of the left leg were also graphed (Figure 13) using the same colour coding as Figure 12.

The graphs of net joint torques and angular velocity (Figure 12 and Figure 13) show three skating 'push-offs' from the left leg. Periods of high torque during the skate contact with the ground were accompanied by low joint angular velocity around 12, 13 and 14 seconds. During the recovery phase at around 12.5 and 13.5 seconds, there were high joint velocities and low torques. If only the flexion/extension actions are considered (red line, Figure 12), the torque was positive at the hip and negative at the knee, however both torques acted together to extend the leg during the contact period. During the first half of the contact phases the flexion/extension angular velocities of the hips and knees (red line, Figure 13) opposed the net joint torques, indicating predominately eccentric muscle action of the hip and knee extensors. During the second half of the contact phases the angular velocity of both the hip and knee changed signs, indicating concentric muscle action in the leg extensor muscle groups.

During the contact phase, in addition to the extension torque there was abduction with external rotation for regular strokes and adduction with internal rotation for cross over strokes. This indicates that not only are the flexor/extensor muscle groups of the legs and hips important in skating, but also the abductor/adductor and internal/external rotator muscle groups are important.

The accuracy of these measurements is unknown. But it is a concerned that the relative motion measured for the knee contained some abduction/adduction movement (blue line, panel two, Figure 13). In a healthy knee this should not be possible and therefore is a measurement error. The erroneous movement probably arose from poor calibration mapping of the IMUs to the thigh and shank segments, especially an error in heading a result of the non-uniform magnetic field during calibration that would allow some flexion/extension to be measured as abduction/adduction. The error could also have been caused by soft tissue artefacts affecting the thigh IMU.

The thigh local segment coordinate system that used as defined by Dumas (Dumas, Cheze, & Verriest, 2007) undoubtedly clouds the issue. The coordinate system uses a set of orthogonal local axes based on bony landmarks with the flexion/extension axis defined normal to the knee-to-hip joint centre vector of the thigh. In reality the flexion/extension axis of the knee is adducted about 10° from the plane normal to the long axis of the thigh. Future work should reduce these errors to get more accurate and unambiguous local net joint torques. Fortunately, when the net joint torques are displayed in the global coordinate system (Video 2: FMC Video\Skate_Rear_Torque.avi) this is not an issue, it is only when the net joint torques and angular velocities are displayed in the local body segment coordinate systems that the data are confusing (Figure 13).

The kinetic analysis of net joint torques was useful for understanding the relative contributions of different muscle groups and their type of action to the skating stroke. Over several strokes it was possible to form an impression of a general trend from this data.

1.7. Variability of inline skating global trajectory

Human movement contains natural variability, even in a simple task. For example, when standing stationary in bipedal stance, natural postural sway is unavoidable (Zatsiorsky & Duarte, 2000). Our athlete skated five laps through a six-gate slalom course described in the previous Section. No two laps were identical (Figure 14), and the variability in the CoM trajectory changed in different parts of the course. The hypothesis to be investigated is that the variability in CoM trajectory through the course is related to how the athlete plans and executes his movements.

This section contains some of the original text contained in the thesis as well as additional information about the trajectory variability experiment, which may be of interest to specific audiences.

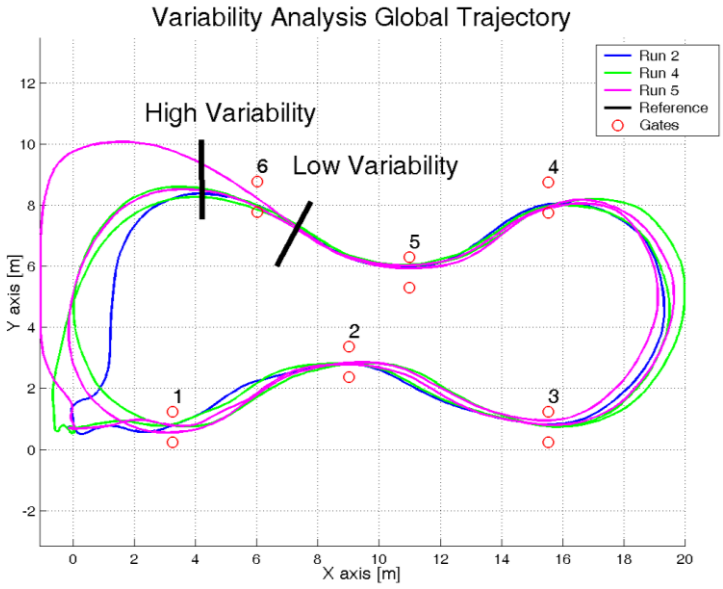

Figure 14: Analysis of variability in global trajectory

1.7.1. Methods and calculations

Using data from the previous inline skating experiment, both the variability in the global trajectory and the variability in the relative approaches to each turn apex were investigated.

Variability in global trajectory

Variability in global trajectory is a measure of how spread-out in space the trajectories from different laps are. Visual inspection of the data spread reveals there is less variability before gate 6 than after gate 6 (Figure 14).

A quantitative measurement of variability in space was developed for inline skating trajectory called the root mean squared (RMS) variability. First the mean trajectory was defined based on the mean location at each point on the course for all laps skated. Then for each point on the mean trajectory the X-Y planer distance between the mean trajectory and the closest point from each lap skated was measured. Finally for each point on the mean trajectory the RMS distance was calculated.

Variability relative to the turn apex

To investigate variability relative to turn apex, the apexes of turns about gates 2 and 5 were aligned. Also turns about gate 5 were rotated by 180° and combined with turns about gate 2. The variability in Y-axis trajectory as X-axis distance from the apex increased was investigated (Figure 15). Y-axis variability was also calculated as time from the apex increased. The variability was calculated as the standard deviation of Y-axis position as a function of both X-axis distances and times from the turn apexes. The time based variability was then transformed into the space domain by using the calculated mean X-axis distance travelled at each time step from the apexes, where the time based variability was calculated. This enabled the two different variability measures to be plotted on the same graph.

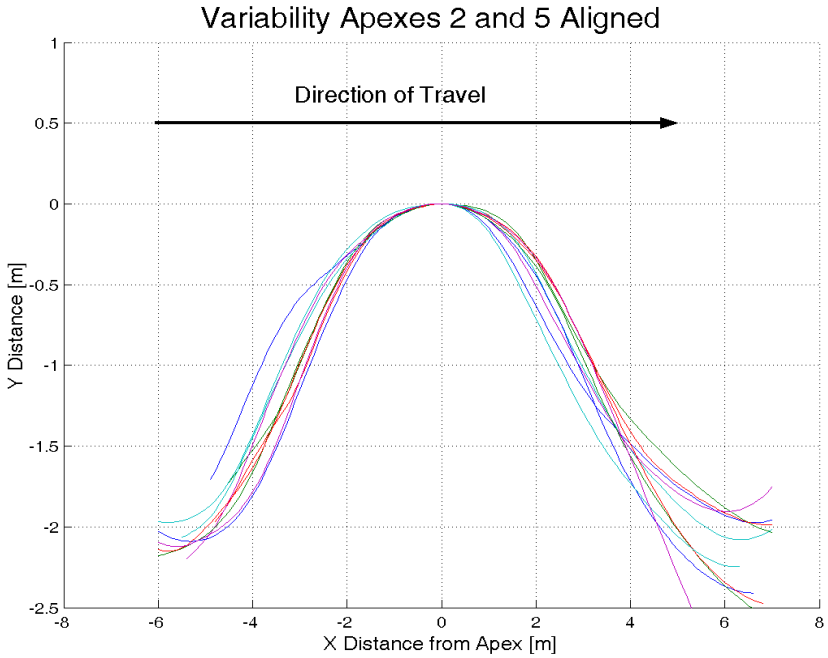

Figure 15: Variability vs. X-axis distance to turn apex, turn 2 and 5

1.7.2. Results and discussion

Variability in trajectory

Variability in trajectory around the course was measured and is displayed below (Figure 16). Where the variability in Figure 16 is low the trajectories of different laps are tightly grouped in Figure 14.

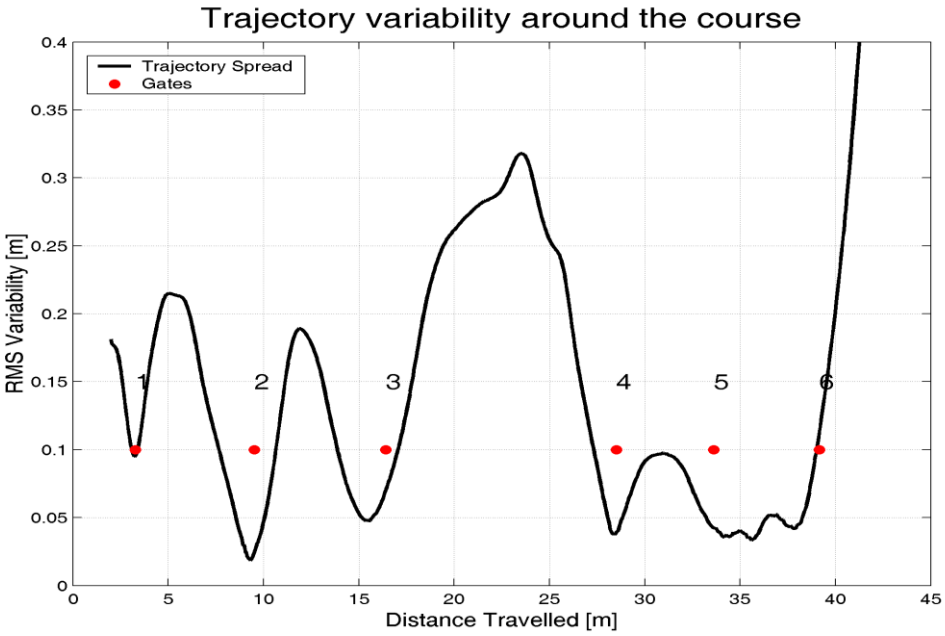

Figure 16: Trajectory variability around the course

In Figure 16 the RMS variability ranges from less than 3cm just before gate 2 to over half a metre after gate 6. In general variability is least just before each gate and on the 'finish straight' between gates 5 and 6.

It was proposed that where the trajectory variability increased (such as between the gates, Figure 14 and Figure 16) the athlete's control of his trajectory decreased and where the variability decreased the athlete's control increased, such as near each gate.

The results suggest that specific checkpoints on the course were very important and the athlete controlled his movements in an attempt to pass close to these points. The checkpoints were generally just before and close to the inside marker of each gate, and would have allowed the athlete to pass efficiently through each gate.

In Figure 16 gate 1 has higher variability than gates 2-5 because the skating starts involving high linear acceleration and the repeat laps with high residual velocity both passed through this gate. Also gate 6 has high variability because it marked the finish of the course. The low variability between gates 5 and 6 shows that the fastest path between the gates on the finish straight was more important than setting up for the end turn after gate 6. These results show that the athlete was capable of using different strategies on different parts of the course, depending on the situation.

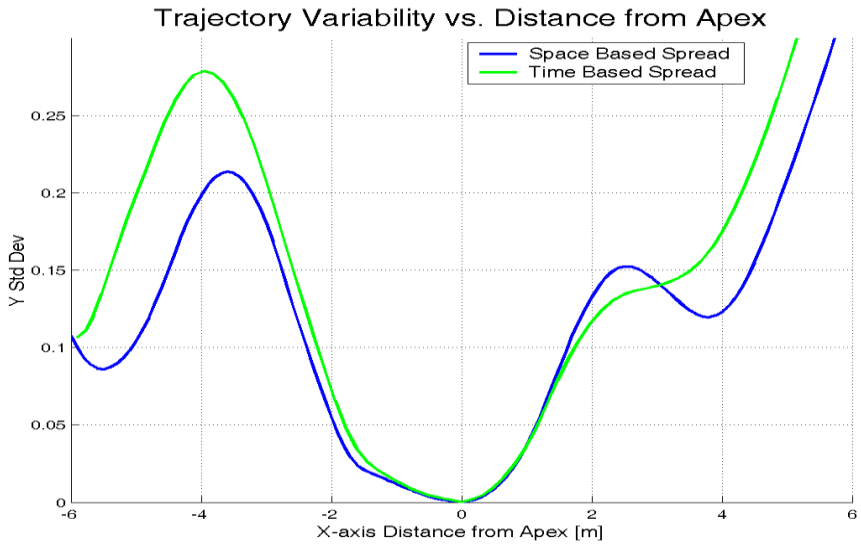

Figure 17: Variability as a function of time and distance from the turn apex

The spread of trajectories about the apexes of turns 2 and 5 was also investigated (Figure 15 and Figure 17). When the apexes are aligned, the global trajectory variability increases faster after the turn apex than before the turn apex. This might give insight into how the athlete executed individual turns irrespective of the overall global strategy, thus enabling turns from different parts of the course to be analysed and compared.

In Figure 17 the trajectory variability one metre before the turn apex (~1.3cm) is a third of the variability one metre after the turn (~4cm). This may imply the athlete used a more consistent approach arc to the turn apex than his exit arc from the turn apex. Therefore, approach was more tightly controlled than exit. It follows that the approach arc that the athlete was using to execute his turns should be investigated. The turn radii of the athlete's turns were calculated by dividing his centre-of-mass velocity squared in the XY-plane (V^2_{XY}) by his centre-of-mass acceleration perpendicular to the velocity vector ($A_{XY\perp}$, Equation 9).

Equation 9 $$Radius = \frac{V_{XY}^2}{A_{XY\perp}}$$

Open radius slalom gate passing strategy

Unexpectedly the turn radius analysis in Figure 18 shows that the athlete does not make the tightest turn either at the gate or at the turn apex. Figure 18 shows the athlete uses a mean turn radius of around 6 metres through gates 2 and 5 (zero distance on the x-axis) and the tightest part of the turn (mean radius of 2-3 metres) generally occurs at lease one metre before and after the gate.

It appears before the turn the athlete aimed not for the gate nor the turn apex, because the least variability was neither at the gate nor turn apex but just before the gate. The athlete appears to have aimed for the start of a repeatable approach arc starting between one and two metres before

the turn apex (Figure 15), which takes him between the gates. The proposed approach arc starts with a tight turn (mean radius 2-3 metres, Figure 18) about 1.5 metres before the gate, which sets the athlete up so he can pass safely through the gates with a more open turn (mean radius ~6 metres). The proposed approach arc also takes the athlete close to a 'check point' generally just before the gate where global variability is least in Figure 16.

The idea of a repeatable approach arc that the athlete is both capable of and aware of has been previously suggested as a way the global trajectory could be constructed by the athlete (LeMaster, 1999). But until now there has been very little data to investigate these ideas.

In Figure 18 while passing through the gates the 6 metre radius turn appears to be controlled in 8 out of the 10 passes; maybe with a feedback loop which results in the observed small ±1metre wave like fluctuations of turn radius. In the other 2 out of the 10 passes the athlete may have lost his balance, set up for the turn poorly, or taken an extra skating stroke resulting in him having to adjust his trajectory while passing through the gate (as indicated by the two spikes in turn radii, up to 14 metres, Figure 18).

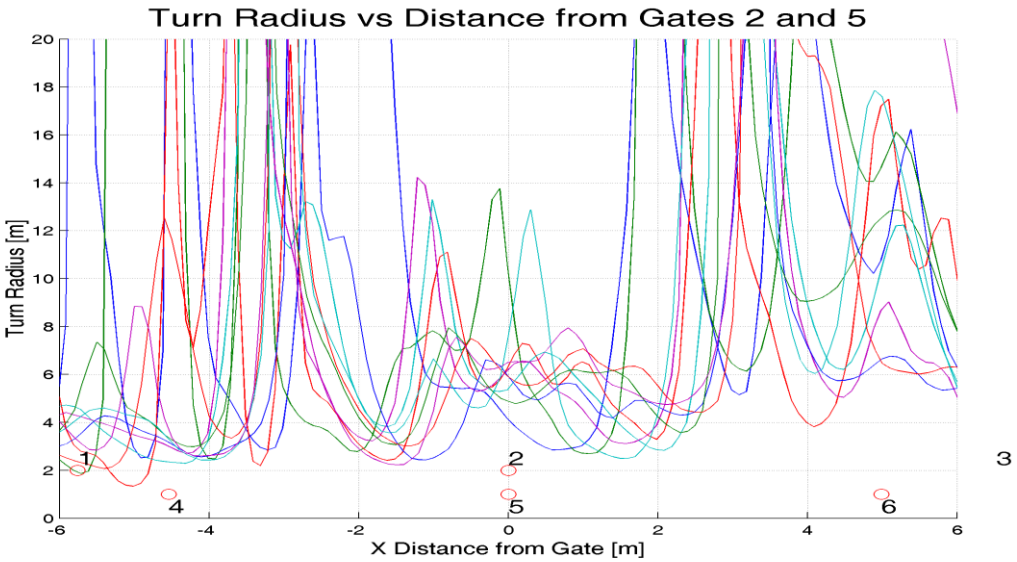

Figure 18: Analysis of turn radius

After the gate the trajectory turn radius is more variable than before the gate. Generally when the athlete travelled slower he took a more direct line turning more tightly closer to the turn apex than before, resulting in a shorter path to the next gate (Figure 15). Some time after the gate the athlete appeared to decrease his turn radius, maybe turning as tightly as he perceived was possible (mean radius 2-3 metres, Figure 18). The minimum turn radius location after the gate was variable, between 0.5 and 2.5 metres, and accounts for the greater variation in trajectory after the gate than before.

The proposed open radius gate passing strategy leaves the athlete a safety margin for error with little performance loss. By setting up with a tight turn before the gate then easing off a little through the gate, if something goes there is slack in the system to make a recover possible. This

strategy also fits well with the timing of his skating strokes; the decrease in turn radii before and after the gate were generally aligned with the end of the skating strokes, and an increase in turn radii was observed as the strokes on the opposite skates began (see Figure 2 on page 9). Therefore the increased variability observed after the turn apex could also be a consequence of the athlete having to adjust his skate stroke timing to set up well for the next gate approach arc.

The open radius gate passing strategy may be slower than the theoretical optimum turn radius; it seems it would be faster to make a tighter turn at the gate while maintaining speed.

Inclination angle controls turn radius?

In skating and skiing the athlete does not have direct control over his trajectory turn radius; instead he can control the local limb movements that create angular acceleration about his anterior posterior axis that result in an inclination from the vertical. The greater the inclination angle the tighter he turns. It would make sense therefore to examine force inclination angle from the vertical with respect to distance from the gate as done in Figure 19.

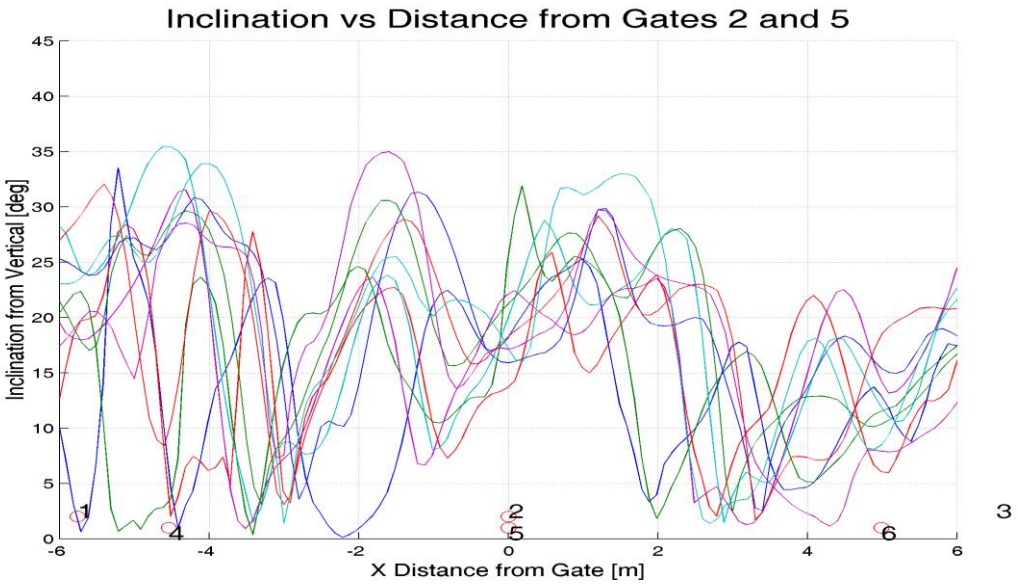

Figure 19: Force inclination from the vertical into the turn

Force inclination angle was calculated by the ratio of vertical to horizontal ground reaction forces perpendicular to the direction of travel (Equation 10).

Equation 10

$$Force\_Inclination = \tan^{-1}\left(\frac{F_{XY\perp}}{F_Z}\right)$$

While the athlete appeared to use a constant radius turn through the gates (Figure 18) he did not use a constant force inclination angle (Figure 19). The data seems to suggest he varied his inclination angle in order to achieve a constant radius trajectory while passing between the gates.

Generally about a metre and a half before and after the gate, force inclination angle peaked. The first inclination peak represents the athlete slowing or checking his angular velocity about the anterior posterior axis (the rate he leans into the turn) by creating an opposing external torque using an impulse of ground reaction force directed inside his CoM trajectory. The second inclination peak after the gate creates enough torque to rotate the athlete out of the turn, though the vertical, and into the next turn. The athlete did not use maximum inclination while passing the gates and this enabled him to create enough external torque about the anterior posterior axis to rotate quickly between the turns and onto the opposite skate edge before the next turn. This interpretation of the results is in agreement with the open radius slalom gate passing strategy described previously.

Turn radius, inclination angles, skating strokes and speed

Further to the previous analysis the question arose: Was control of turn radius more important to the athlete than inclination angle? The athlete's control of radius and inclination over a single end turn was investigated (between gates 3 & 4, Figure 14). Over the end turn the distance was long enough for speed to fluctuate as shown in Figure 20 (Time ~ 15s to 17s).

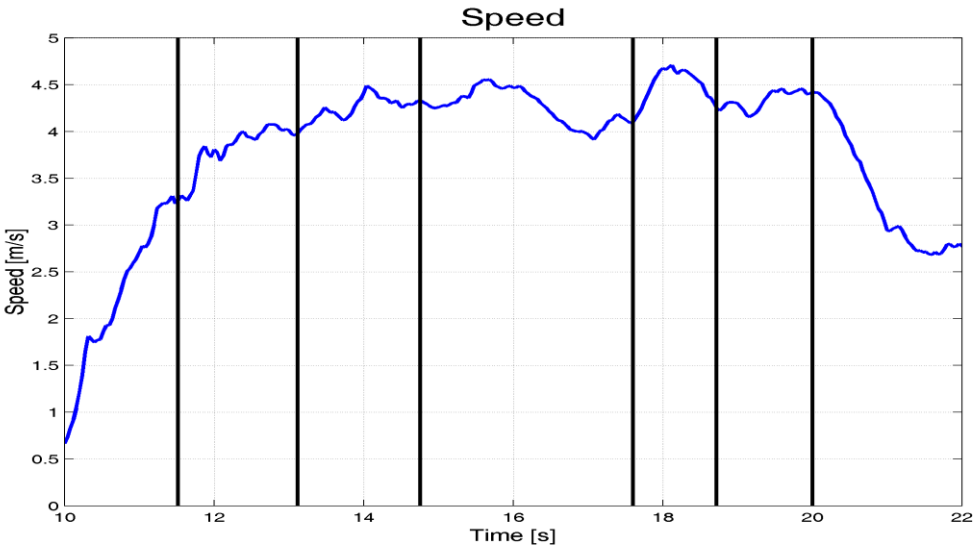

Figure 20: Athlete speed through one lap of the course.

Figure 21 shows the physical inclination defined as the angle between the mean skate centre of pressure (CoP) and the athlete's CoM about direction of CoM travel. However this was highly variable due to effects of skating strokes combining with the athlete's global trajectory. The effects of the skating strokes on physical inclination can be observed about the end turn of the course in Run 2 (Figure 21, Time ~ 15s to 17s). Four distinct skating strokes were executed and correspond to the four peaks in inclination angle.

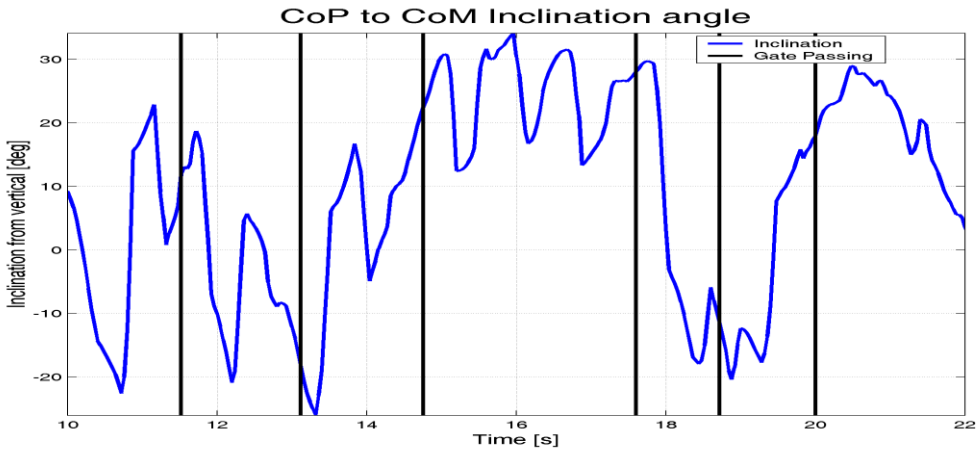

Figure 21: Physical inclination based on mean CoP and CoM location

Force inclination through the end turn (Figure 22, Time ~ 15s to 17s) like the previous analysis of slalom turns (Figure 19) initially appears more variable than turn radius through the end turn (Figure 23, Time ~ 15s to 17s). But if, for a moment, the high frequency components, the mean force inclination appears to be constant even though speed through the turn has varies from 3.9m/s to 4.6m/s. The high frequency components could be explained by the need to take four skating strokes, a trajectory correction half way though the turn (spike in force inclination and radius at time ~ 16s) and the need to maintain dynamic balance about the anterioposterior axis.

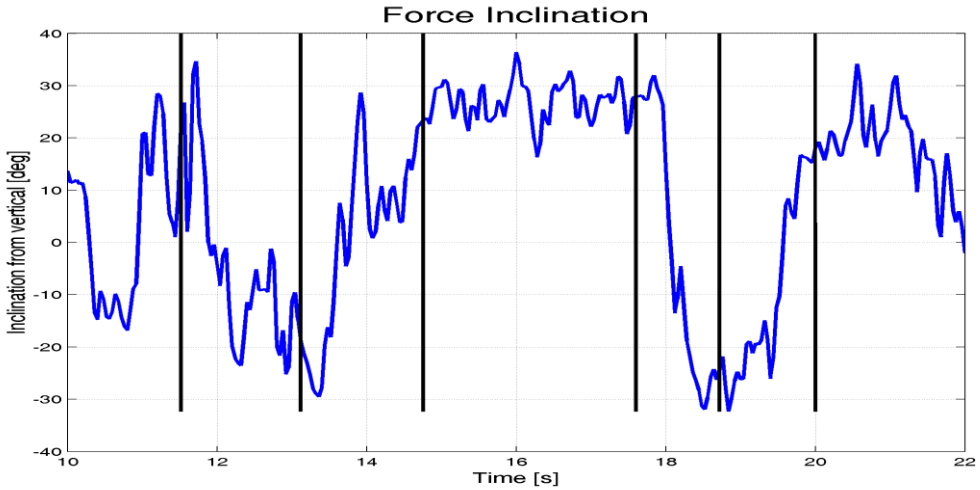

Figure 22: Force inclination through a complete lap of the course.

These analyses suggests that the athlete controls his trajectory in part by selecting a target force inclination angle for a turn, but it is difficult to observe this in the data due to the high frequency components in the inclination measurement. The constant turn radius previously observed might then only be a consequence of constant target inclination angle combined with constant turn speed. If so this would explain the small downward trend in end turn radii, (Figure 23, Time ~ 15s to 17s) that may be correlated to end turn speed (Figure 20) but is obscured by a trajectory correction at around 16 seconds.

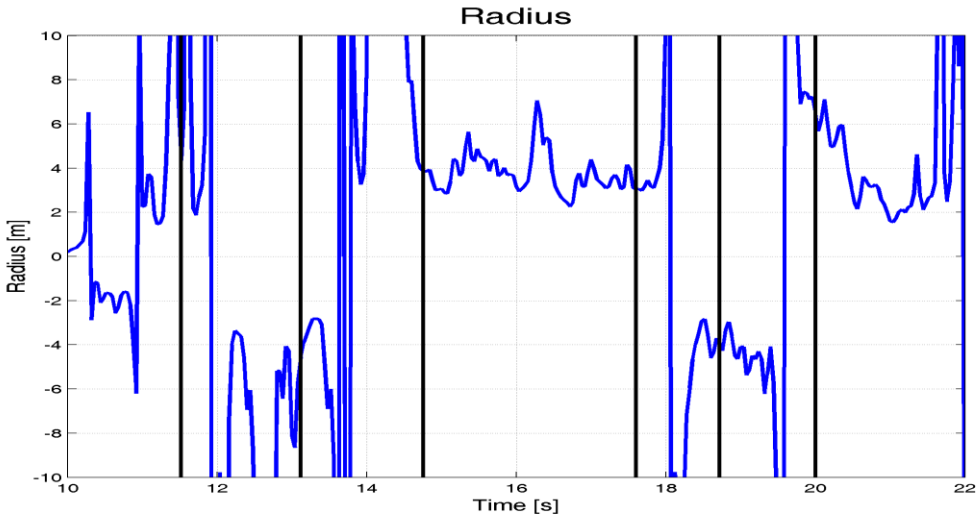

Figure 23: Turn radius through one lap of the course.

Using consistent turn radii while passing between the gates is likely to be important because the task has a high spatial component. Reducing the variability of turn radii together with a series of spatial checkpoints reduces the athlete's degrees of freedom and would simplify the control mechanisms required to successfully skate through the course.

Using a target force inclination angle for each turn instead of a constant radius has the same effect of simplifying control. It is not possible from this data to determine which of the two parameters (turn radii or force inclination angle) was more important to the athlete and it is quite possible both parameters were important. Force inclination angle is also directly related to the physical friction cone angle limit of 31° previously calculated, Figure 5.16 of the thesis. The consistency of the data falling within the friction cone suggests the athlete was keenly aware of maximum force inclination angle.

This raises the question if turn radius and/or target force inclination angle is controlled how does the athlete sense either of these parameters? The athlete could possibly sense turn radius indirectly through changes in visual field including the gate makers. The athlete could also possibly sense force inclination through acceleration acting on his vestibular system. The athlete could also sense absolute head inclination by rotation of the visual horizon. But further investigation of this is beyond the scope of this thesis.

More discussion about control mechanisms

The two times that turn control was lost, the turn radius spiked above 12m (green and light blue spikes just before and after X~0, Figure 18) but the athlete quickly recovered the trajectory radius with an increase in inclination angle above 30º (green narrow spike and light blue broad spike above 30° after X=0, Figure 19). The time between the spikes of these two graphs (~60ms) might give an estimate of how quickly the athlete's mechanical system reacted to small perturbations during this complex skilled movement. If so 60ms is very quick indicating the reaction to the perturbation is initially controlled by the mechanical considerations of the system (like a gyroscope). If the athlete's skate slips while turning the horizontal ground reaction forces are

momentarily reduced, which automatically makes the athlete incline more resulting in a tighter turn to maintain balance. Alternatively, spinal feedback loops might be activated by such stimulus as the loss of tension in the muscle spindles of the loaded leg, and some fast acting correction could be made.

Both the time from turn apex and distance from turn apex trajectory variability are similar (Figure 17). If time to turn apex was also a factor influencing the athlete's control of the turn, it would be consistent with the observation of gannets folding their wings at the same time to contact with the water surface, but not necessarily with distance from the water surface (Lee & Reddish, 1981). It would also be consistent with the fact the athlete had to lean into each turn, and because he behaved more or less like as inverted pendulum (moving rhythmically between turns of similar inclination angle), it would take him the about same amount of time to lean into each turn. Because the athlete was travelling at a fairly consistent velocity through the course, time to contact and distance to contact were highly correlated. It is therefore impossible from this information to separate the two effects.

Final caveats

It should be noted that while the athlete was encouraged to skate quickly through the gates he was not instructed to skate as quickly as possible and his strategy may have been influenced by the high capital value of the fusion motion capture system components. It is quite possible minimum course time was not his only consideration.

If there is enough cross over between inline skating and slalom skier technique then these results might be interesting to slalom athletes. Possibly ski race performance may be limited by the athlete's pre-determined perception of a safe passing trajectory through each gate. If so, some training should focus on decreasing the perceived limits of turn radii and increasing the inclination angle used. During training non-uniform gate spacing should be used sometimes to challenge the athlete to use a variety of strategies and turn radii/inclination angle. Dependant on the course position, this type of control is possible as demonstrated by our athlete who used a straight finish to gate 6. Also markers could be placed on the course to help the athlete identify the optimum location to start the entry arc to each turn. Additional markers could also identify any global checkpoints, over which the athlete should pass, as well as passing close to the inside marker of the course gates.

This pilot study has revealed a number of possible hypotheses and in the future a more detailed study is required to confirm the findings.

1.8. Simulation of athlete specific optimum trajectories

Inline skating through a set of slalom gates has many similarities to skiing. It is also easier to model because the simulated athlete does not have to choose either a carving turn or a skidding turn and can make turns of any radius on the skates. This chapter is a step towards the thesis objective:

"Optimisation of an athlete movement in alpine ski racing"

The optimum (fastest) global trajectory of our athlete through the course he skated was modelled. Parameters measured from the athlete's performance were used to drive the simulation. The athlete was modelled as a single ridged body using the mean measured inertial properties of the athlete.

This section contains some of the original text contained in the thesis as well as additional information about the simulation experiment, which may be of interest to specific audiences.

1.8.1. Methods

Simulation constraints

The simulated trajectory was based on a simplified model of the athlete's whole body motion. The effects of individual limb motions or foot strokes were not considered. Instead the following parameters were extracted from the athlete's performance to drive the simulation using the fusion motion capture data:

1. Maximum inclination while cornering (~31°). The maximum inclination and the athlete's mass (68kg) determine the maximum horizontal forces (*HGRF* ~ 440N) the athlete can produce and therefore the maximum speed (*Speed*) he can make a turn of any given radius (*Radius*, Equation 11). The maximum inclination was based on the 'friction cone', the relationship between the horizontal and vertical ground reaction forces described previously (Figure 5.16 of the thesis).

Equation 11 $$Speed = \sqrt{\frac{HGRF*Radius}{Mass}}$$

2. Maximum angular acceleration about the direction of travel (α~5rad.s^{-2} or ~300°.s^{-2}); The angular acceleration determines how quickly the athlete can rotate from edge to edge between left and right turns. 'Bang bang' control was assumed (the athlete accelerates and brakes his rotation with no rest to move from edge to edge) to calculate minimum time of rotation (*Rot_Time*) based on the change in inclination angle between two consecutive turns (θ_{Start} and θ_{End}, Equation 12). The turn inclination angles were dependant on the athlete's turn speeds and turn radii and gravity (*G*, Equation 13). The maximum angular acceleration was determined by the root mean square of the angular acceleration about the direction of travel (Figure 24), which was calculated by dividing the previously calculated rate of change of angular momentum (Figure 5) by the instantaneous whole body moment of inertia.

Equation 12 $$Rot\_Time = 2\sqrt{\frac{\theta_{Start} + \theta_{End}}{\alpha}}$$

Equation 13 $$\theta = \tan^{-1}\left(\frac{Speed^2}{Radius * g}\right)$$

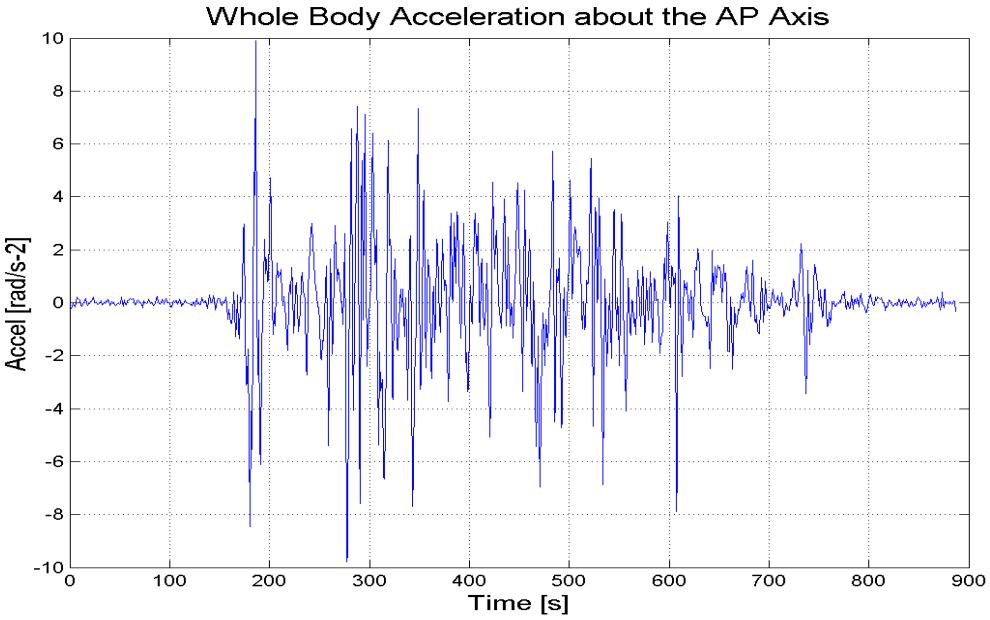

Figure 24: Calculated angular acceleration about the direction of travel

3. The calculated coefficients of wind drag and bearing friction (K_{Drag} = 0.58 Ns^2m^{-2} and $K_{Friction}$ = 0.016, from the previous chapter.

4. The athlete's power curve defined by the force-velocity relationship (Figure 25); the figure of the fusion motion capture data shows the faster the athlete skated the less force was available to increase his speed. This relationship was approximated by a linear equation (Equation 14) fitted to the data from Figure 25. The linear equation represents a line that creates a boundary on the axes that encapsulates 95% of the data points.

Equation 14 $$Force = 716 - 133 * Velocity \quad \textbf{(N)}$$

5. The final constraint was the location of the course gates, through which the trajectory was required to pass.

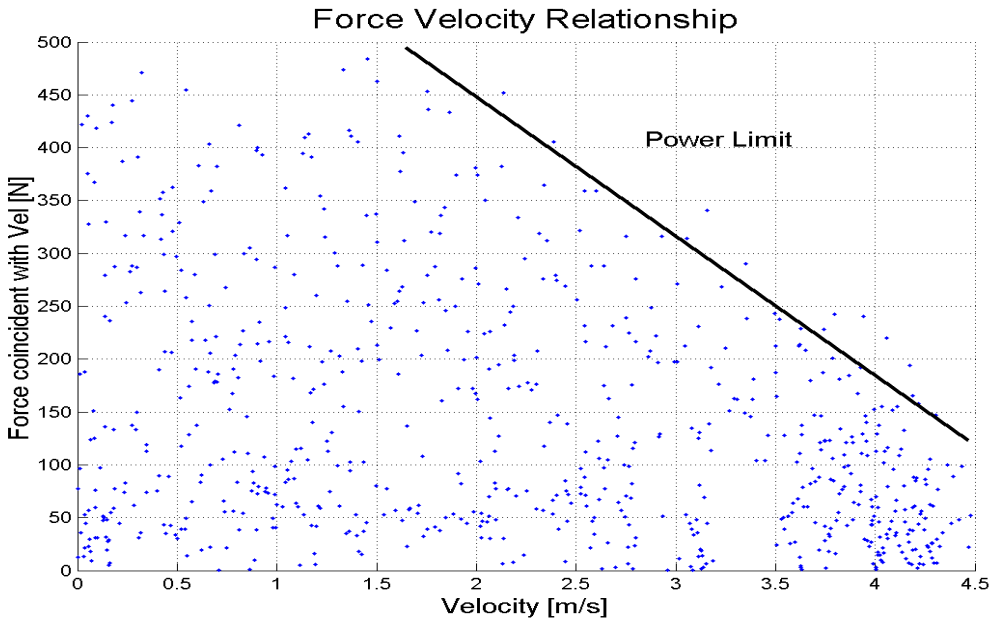

Figure 25: The force-velocity relationship

Optimisation of the global trajectory

MATLAB's constrained non-linear minimisation function was used to find the minimum time trajectory that passed between the course gates. The trajectory was found using MATLAB functions written to calculate the time through the course with different combinations of turn apexes and turn radii. Turn apex and turn radii were chosen as control parameters because this agrees the observations of global trajectory variability in the previous chapter.

MATLAB's constrained non-linear minimisation function passed the control parameters of turn apexes and radii to the trajectory functions, which returned a course time and information if course constraints were exceeded. The starting guess was a trajectory that passed through the inside of each gate with a turn radius of two metres. After 22 iterations of the minimisation function and 786 executions of the trajectory functions the minimum time trajectory was found. It took about 120 seconds using a laptop (Celeron M 1.60GHz processor) to solve for the turn apexes and radii that produced a minimum time trajectory. A variety of starting guesses were used but this was the best result.

The MATLAB functions used to calculate course time used the following procedures: Given the set of turn apexes and turn radii the global trajectory was solved piecewise from turn apex to turn apex. The global trajectory between consecutive apexes was approximated by two circular arcs connected by a straight line (Figure 26).

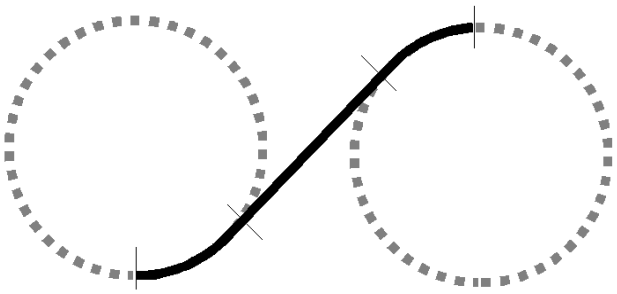

Figure 26: Simulated trajectory between two apexes

The maximum speed at about each arc was limited by the simulated athlete's ability to produce incline and produce horizontal ground reaction forces (Equation 11). The simulated athlete's speed between the arcs was limited by the length of the connecting line and the minimum time required rotating from edge to edge between the arcs according to Equation 12. Further more the simulated athlete's speed had to be continuous. Starting from the 'slowest maximum speed constraint', bang-bang control was used to either accelerate the simulated athlete using available ground reaction force power or decelerate the athlete due to wind drag and bearing friction. If during the calculation process the simulated athlete could not brake fast enough to meet a speed constraint, then calculations were re-iterated starting from the new 'slowest maximum speed constraint' to ensure the simulated speed profile was continuous.

1.8.2. Results and discussion

The simulation was successful in defining a minimum time trajectory through the course. The simulated athlete was able to pass through the course in 10.87 seconds (Figure 27). This was faster than the best lap time by our athlete, 13.60 seconds, and represents a 2.73 second or 20% improvement.

In a surprise result: the simulated athlete achieved the improvement by skating slower, which enabled him to take a shorter path with tighter radius turns. The simulation consisted of eight turns through six gates because two extra turns were required to make the end turns possible. The two extra turns will be named end turn 1 and 2 for the purposes of this discussion. The main difference between the simulated athlete and the real athlete is in the execution of the end turns. For turns 1,3,4 and 6 the simulated athlete moved the turn apexes closer to the centre of the course and this allowed both end turns to be moved inwards and the trajectory shortened (Figure 27). However the trade-off was a slower maximum speed (4.2 m/s for the simulation reduced from 4.6m/s for the real athlete) limited by his maximum inclination angle (31°) and the tighter turn radius. It appears the athlete could achieve the resulting 20% time reduction with less effort because less skating power would be required to reach the slower optimum speed, but tighter trajectory control would be required.

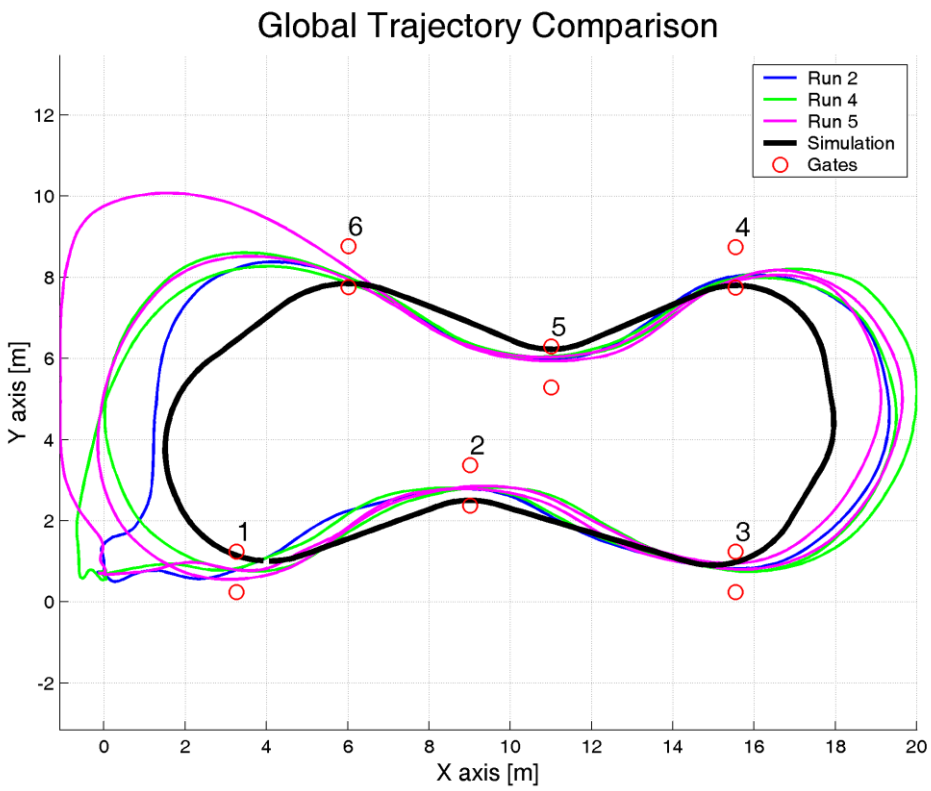

Figure 27: Simulated trajectory vs. five actual laps through the course

The simulated athlete's trajectory consisted of a slow section (between gate 2 and gate 5, mean speed 3.7 m/s) and a fast section (between gate 6 and gate 1, mean speed 4 m/s). The turn radii through the slow turns are consistently tighter (2.18-2.27, Table 1) than the turn radii through the fast section (2.45-2.76 m).

Turn	**Gate 1**	**Gate 2**	**Gate 3**	**End 1**	**Gate 4**	**Gate 5**	**Gate 6**	**End 2**
Radii [m]	2.45	2.19	2.19	2.27	2.21	2.18	2.74	2.76

Table 1: Simulated trajectory turn radii

The simulated results appear almost too good to be true and care should be taken in interpreting these results because: The solution may be a local optimum, and not the absolute minimum time trajectory. The solution may also be a result of artefacts introduced because of the simplicity of the model, which does not model individual foot strokes or how the athlete creates an external torque to rotate from edge to edge between the turns. The MATLAB simulation also ran into an extremely frustrating problem: As the simulation approached the optimum it would freeze for no apparent reason, in which case the simulation was re-started and terminated just before it would have frozen and a less than optimum solution was reported. In hindsight the freezing might have been because the numerical solution used discrete time steps. Although the solution presented initially appears plausible it should be tested. A real athlete could be trained to skate through the course using extra visual markers to mark the simulated optimum apex locations.

In any case the process of simulating the athlete's global trajectory offers insights into the constraints that limit athletic performance. Through the straight sections of our course that the athlete's maximum speed should be 5.18m/s by the solution of a quadratic equation (Equation 15). Equation 15 is formed by combining equations Equation 14 for accelerating force with the equations for bearing friction and wind drag (Equations 5.10 and 5.11 of the thesis). The maximum speed is reached when the resultant force acting on the athlete is zero.

Equation 15 $$(716 - K_{Friction} * Mass * G) - 133 * Speed - K_{Drag} * Speed^2 = 0$$

The true athlete's maximum speed through our course was 4.6m/s, less than the theoretical maximum, 5.18m/s, but more than our simulated athlete's maximum speed of 4.2 m/s, which indicates the athlete's performance, was primarily limited by the tight gate spacing. His performance was limited by his ability to incline into each turn, described by the friction cone (in Figure 5.16 of the thesis) and his ability to rotate quickly from edge to edge between the turns limited by his angular acceleration described in Figure 24, but not by the power he could generate through his skating stroke described by Figure 25.

The promising results suggest this type of simulation will be useful for the analysis of optimum ski racing trajectories in the future.

1.9. Bibliography

Dumas, R., Cheze, J., & Verriest, P. (2007). Adjustments to McConville et al. and Young et al. body segment inertial parameters. *Journal of Biomechanics, 40*, 543-553.

Kaps, P., Nachbauer, W., & Mossner, M. (1996). Determination of kinetic friction and drag area in alpine skiing. *Ski Trauma and Skiing Safety ASTM, 10*, 165-177.

Lee, D. N., & Reddish, P. E. (1981). Plummeting gannets: a paradigm of ecological optics. *Nature, 293*, 293-294.

LeMaster, R. (1999). *The Skiers Edge*. Auckland: Human Kinetics.

Shimbo, M. (1971). *Friction of snow on ski soles, unwaxed and waxed*. Tokyo: Hitachi.

Spring, E., Savolainen, S., Erkkila, J., Hamalainen, T., & Pihkala, P. (1988). Drag Area of a Cross-Country Skier. *Journal of Applied Biomechanics, 4*, 103-113.

van Ingen Schenau, G. J. (1982). The influence of air friction in speed skating. *Journal of Biomechanics, 15*(6), 449-458.

Zatsiorsky, V., & Duarte, M. (2000). Rambling and Trembling in Quiet Standing. *Motor Control, 4*, 185-200.